Journal of Computational Physics 228 (2009) 4400–4434

Contents lists available at ScienceDirect

Journal of Computational Physics

journal homepage: www.elsevier.com/locate/jcp

Coupled fluid–structure solver: The case of shock wave impact on monolithic and composite material plates

Minwei Gong, Yiannis Andreopoulos *

Department of Mechanical Engineering, The City College of the City University of New York, Convent Avenue and 140th Street, New York, NY 10031, United States

ARTICLE INFO

Article history:
Received 28 June 2008
Received in revised form 10 March 2009
Accepted 10 March 2009
Available online 20 March 2009

Keywords:
Fluid–structure interactions
Adaptive mesh
Composite materials
Shock waves
Modes
Resonance
Acoustics
Aeroelastic response

ABSTRACT

An unstructured adaptive mesh flow solver, a finite element structure solver and a moving mesh algorithm were implemented in the numerical simulation of the interaction between a shock wave and a structure. In the past, this interaction is mostly considered as one-way in the sense that the shock causes a transient load on the structure while it is reflected uneffected by the impact. A fully coupled approach was implemented in the present work which can account for the effects associated with a mutual interaction. This approach included a compressible flow Eulerian solver of second order accuracy in finite volume formulation for the fluid and a Langargian solver in finite element formulation for the solid structure. A novel implementation of advancing front moving mesh algorithm was made possible with the introduction of a flexible and efficient *quad-edge* data structure. Adaptive mesh refinement was introduced into the flow solver for improved accuracy as well. Numerical results are further validated by theoretical analysis, experimental data and results from other numerical simulations. Grid dependency study was performed and results showed that the physical phenomena and quantities were independent of the numerical grid chosen in the simulations. The results illuminated complicated flow phenomena and structure vibration patterns, which in order to be detected experimentally require capabilities beyond those of the current experimental techniques. The numerical simulations also successfully modelled the aero-acoustic damping effects on the structure, which do not exist in previous numerical models. Further analysis of the results showed that the mutual interaction is not linear and that the non-linearity arises because the wave propagation in the fluid is not linear and it cascades a non-linear and non-uniform loading on the plate. Non-linearity intensifies when the plate is vibrating at high frequency while the wave propagation speed is low.

1. Introduction

Shock or blast wave loading on elastic structures has been investigated for many years in the past. Hopkinson [1] contributed the first published work on the subject while Taylor [2] developed a solution for one-dimensional wave impinging a free-standing plate to compute the momentum transmitted to the plate by the shock pulse. The impingement of these waves on a structure is associated with a reflection of the wave off the surface of the structure followed by a substantial transient aerodynamic load, which can cause significant deformation of the structure. In addition, a complex aeroelastic interaction between the blast wave and the structure develops that can induce reverberation within an enclosure, which can cause substantial overpressure through multiple reflections of the wave. This problem is of particular importance in the new design of

* Corresponding author. Tel.: +1 212 650 5206; fax: +1 212 650 8013.
E-mail address: andre@ccny.cuny.edu (Y. Andreopoulos).

0021-9991/$ - see front matter © 2009 Elsevier Inc. All rights reserved.
doi:10.1016/j.jcp.2009.03.009

building structures and vehicles with composite materials where maximum survivability is sought. In the past, this interaction has been considered as "one-way" only, i.e. the impacting shock wave creates a load which deforms the structure. However, this deformation affects the shock wave reflection and therefore the interaction is a two-way process. The mutual interaction between a blast or shock wave and an elastic structure is the subject of the present contribution which is a continuation of our experimental work published in Gong and Andreopoulos [3] hereafter mentioned as G&A and is based on the Thesis research by Gong [4]. The work of G&A showed a substantial difference in the behavior of monolithic and composite materials under shock wave loading. Due to the elastic deformation of the plates and their reverberation, strong acoustic waves were generated on the external side of the impact which carry a significant signature of the plates' properties. One of the most surprising result of this experimental work is that composite plates were found to suppress several of the modes of the wave patterns while metallic ones demonstrate a rich variety of interacting modes. The amplitude of the excited acoustic waves, however, was higher in the case of composite plates than in the case of steel plates. The frequency content of the strain signals on the surface of composite plates was not always the same with the content of the surface acceleration measured in free vibration experiments. The experiments of G&A also indicated that damping played an important role during the interaction, especially in the case of composite plate.

The objective of the present work is to develop and validate a fluid–structure solver which will incorporate the mutual interaction between the incoming shock wave and the structure. This mutual interaction is particularly important in blast occurring inside enclosures where multiple shock wave reflections take place which are then affected by the deformation of the structures. In that respect the numerical simulation of the blast and structure interaction is essentially a fluid–structure interaction problem similar to the computational aeroelasticity problem, hereafter referred as CAE. In this manuscript, the three major models pertaining to CAE, namely, flow solver, structure solver and moving mesh algorithm, are analyzed and thereby suitable models are chosen to simulate the fluid–structure interaction.

Houlston et al. [5] investigated the structural response of ship panels to free field air-blast explosions. Gupta et al. [6] conducted a single-degree-of-freedom elastodynamic analysis of the response of a rectangular plate subjected to an explosive blast while Beshara et al. [7] investigated the prediction of dynamic effects of unconfined explosions needed for the structural analysis of blast-loaded above-ground structures. Turkmen and Mecitoglu [8,9] carried out a study on the dynamic behavior of laminated composite plates subjected to blast loading. The behavior of steel plates in various configurations under air blast loading was studied experimentally and computationally in [10,11]. All those aforementioned investigations of the response of a structure to blast or shock wave impact have been focussed on the structure alone. However, as was mentioned earlier, the interaction between the blast and the structure is mutual, particularly when the size of structure is of small scale. During the interaction, the structure is deformed by the loading and its deformation affects the blast reflection itself on the inner side of the structure where the blast impacts and excites acoustic disturbances which may be quite strong and may be developing into a weak shock wave on the outer side. The aeroelastic coupling between the structure and the blast loading is not fully understood. In weak interactions between acoustic disturbances and flexible structures linear and non-linear acoustic waves have been observed by many authors as a result of harmonic vibrations of these structures [12,13]. However, the complicated resonance caused by the blast loading on the structure and the flow phenomena associated with sound excitation and shock waves reflections mentioned above have not been fully investigated. Xue and Hutchinson [14,15] studied the *quasi-static* dynamic responses of clamped circular sandwich plates subject to uniformly distributed impulsive loads by neglecting the effects of fluid–structure interaction.

The present research focuses on the development and verification of a computational code capable of predicting the coupled aeroelastic response of metallic/monolithic and composite materials to blast or shock wave impact. In particularly, the objective of the present work is to simulate the experiments of G&A in which planar shock waves were impacting in "face-on" configuration flat plates mounted at the end of a large size shock tube (see Fig. 1). In these experiments, one aluminum plate, one stainless steal plate and several composite plates were tested. Miniature semi-conductor strain-gauges of high frequency response were employed to measure locally the strain on the exterior side of the plates and high frequency response pressure transducers were used to measure time-dependent wall and total pressure. The work of G&A also includes calculations to determine the modal response of the plates under impulse loading. The classical Poisson–Kirchoff theory for thin

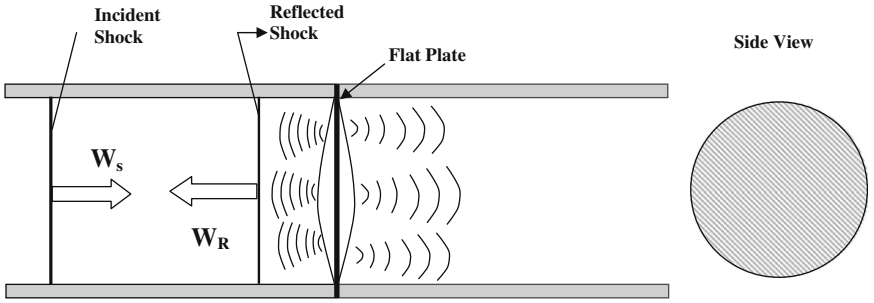

Fig. 1. Flow geometry of a plane shock wave interaction with a thin flat plate and sound waves excitation through shock impingement.

plates under axisymmetric or non-axisymmetric conditions was used for modal analysis and extracting the vibration patterns. A time-dependent analytical solution was obtained which was employed to model the dynamic response of a plate under shock loading. A coupled system of equations between fluid and solid phases of monolithic materials was also used in which the fluid phase was modelled through the wave equation model. Free vibration (no damping) and forced vibration finite element analysis was also carried out. These two cases provided predictions in good agreement with the measured values of modal frequencies. The coupled fluid–structure calculations yielded a lower eigenfrequency compared with that of the uncoupled calculation, which is a result of the added virtual mass in the couple solution. In the case of higher modes, the classical Poisson–Kirchoff theory and the coupled free vibration analysis provided reasonable agreement with the experimental data.

2. Governing equations

The Euler equations define a system of non-linear, hyperbolic, first order conservation laws which describe the flow of an inviscid, compressible fluid. The Euler equations in two dimensions for an arbitrary control volume Ω, fixed in space and bounded by a closed surface **S** with the outward vector d**S** can be expressed as:

$$\frac{\partial}{\partial t}\int_{\Omega} U\,\mathrm{d}V - \int_{\partial\Omega} F\cdot\mathrm{d}S_x - \int_{\partial\Omega} G\cdot\mathrm{d}S_y \tag{1}$$

where the conservative state vector **U** and the flux functions **F** and **G** are defined as

$$\mathbf{U}=\begin{bmatrix}\rho\\ \rho u\\ \rho v\\ \rho e\end{bmatrix},\quad \mathbf{F}=\begin{bmatrix}\rho u\\ \rho u^2+p\\ \rho uv\\ (\rho e+p)u\end{bmatrix},\quad \mathbf{G}=\begin{bmatrix}\rho v\\ \rho uv\\ \rho v^2+p\\ (\rho e+p)v\end{bmatrix} \tag{2}$$

where ρ is the density, u and v are the velocity components, e is the internal energy, and p is the static pressure given by

$$p=(\gamma-1)[e-((\rho u)^2+(\rho v)^2)/2\rho)] \tag{3}$$

The system of equations written above define the conservation laws for mass, momentum and energy. The Euler equations are written in conservative formulation which is very well suited for the finite volume method (FVM) as control volumes are defined and their quantities are conserved within the control volume.

First, the geometric domain (the flow field) under investigation is subdivided into control volumes Ω_i through an appropriate grid. When the cells are chosen as the control volumes, it is cell-centered, if the dual of a given grid is used, it is called as vertex-based, under which there is a volume corresponding to each vertex of the original grid.

Second, in order to approximate the integrals of Eq. (1), the conservation variable **U** is represented by cell-wise constant values $\mathbf{U}_i$

$$\frac{\partial}{\partial t}\int_{\Omega_i}\mathbf{U}\,\mathrm{d}V \approx |\Omega_i|\frac{\partial}{\partial t}\mathbf{U}_i \quad 1\leqslant i\leqslant N \tag{4}$$

where $|\Omega_i|$ is the volume of Ω_i. It should also be noticed that $\mathbf{U}_i$ is approximately equal to the integral of the true solution and therefore it can be considered as a conservative approximation. Thus, Euler equations under the above discretization leads to a system of N ordinary differential equations in t

$$\frac{\partial}{\partial t}U_i = -\frac{1}{|\Omega_i|}\int_{\partial\Omega_i} F\cdot\mathrm{d}S_x - \frac{1}{|\Omega_i|}\int_{\partial\Omega_i} G\cdot\mathrm{d}S_y = -\frac{1}{|\Omega_i|}\int_{\partial\Omega_i}\hat{F}\cdot\mathrm{d}S \quad 1\leqslant i\leqslant N$$

Here we define $\hat{\mathbf{F}}=\mathbf{F}+\mathbf{G}$ for notation simplicity.

A simple time integration scheme can be obtained by replacing the time derivative $\frac{\partial}{\partial t}\mathbf{U}_i$ by a simple forward difference and evaluating the flux residual at the current level

$$\frac{\partial}{\partial t}\mathbf{U}_i = \frac{\mathbf{U}_i^{n+1}-\mathbf{U}_i^n}{\Delta t} = -\frac{1}{|\Omega_i|}\int_{\partial\Omega_i}\hat{\mathbf{F}}\cdot\mathrm{d}\mathbf{S} \quad 1\leqslant i\leqslant N \tag{5}$$

This corresponds to a single-stage explicit scheme, since updates are obtained from one evaluation of currently available quantities. Explicit Runge–Kutta schemes could also be used in order to achieve time accuracy, a fourth stage Runge–Kutta scheme could be written as:

$$\begin{aligned} &W_i^0 = U_i^n\\ &W_i^k = W_i^0 + \alpha_k\Delta t F(W_i^{k-1}) \quad \text{for } k=1\cdots 4\\ &U_i^{n+1} = W_i^4 \end{aligned} \tag{6}$$

where F is defined as

$$F = -\frac{1}{|\Omega_i|}\int_{\partial\Omega_i}\hat{F}\cdot \mathrm{d}S$$

for notation simplicity. The α_k are chosen as the following:

$$\alpha_1 = 0.11, \quad \alpha_2 = 0.2766, \quad \alpha_3 = 0.5, \quad \alpha_4 = 1.0$$

Δt is constrained by the *Courant Friedrick Leavy condition*, which is that the domain of dependency of the numerical method includes the physical domain of dependency of the equation: information in the numerical scheme must include information influencing the physical flow. This results in:

$$\Delta t \leqslant \Delta x/|\lambda_{max}| \tag{7}$$

where λ_{max} is the maximum wave speed, Δx is the control volume length, which will be addressed later.

3. High resolution schemes

While the upwind scheme is highly stable, it needs to be modified to high order if high resolution is desired. There are three major families of high resolution schemes, MUSCL van Leer [31], non-MUSCL TVD (e.g. MINIMOD Harten [32]), ENO (essentially non-oscillatory) Harten et al. [33] and WENO (weighted ENO) Jiang and Shu [34] schemes. Van Leer [31] introduced the idea of modifying the piecewise constant data in the first order Godunov method to a achieve higher order of accuracy. This approach has become known as the MUSCL or variable extrapolation approach, while MUSCL stands for *monotone upstream-centered scheme* for the conservation laws, where monotonicity in MUSCL is enforced through a limiter function applied to a piecewise polynomial flux reconstruction procedure. Harten [32] expressed monotonicity as a measure of discrete variation in the solution fields, which was named as total variational diminishing (TVD). In the non-MUSCL TVD schemes, the higher order extensions are carried out by embedding a flux limiter directly into the flux function. In ENO schemes, the accuracy is increased through the use of higher order interpolation functions and do not employ any type of limiter functions.

However, the application of higher order schemes to multi-dimensional unstructured mesh is not the direct extension of 1D scheme due to the fact that most of the mathematical proofs in regards to these high resolution schemes have only been carried out for scalar 1D non-linear equations. It also has been proved that TVD schemes cannot be formally second order accurate in two or three dimensions. A number of TVD/MUSCL approaches for unstructured mesh have been implemented in the current research as illustrated and reviewed in Darwish and Moukalled [35] and Hubbart [36]. Among them the implementation that follows the Barth [37] and Barth and Jesperson scheme [38] has been the most successful.

In the Barth and Jesperson scheme, the linear reconstruction of the control volume value Φ_p satisfies:

$$min(\Phi_N, \Phi_P) \leqslant R_P(\mathbf{r}_j) \leqslant max(\Phi_N, \Phi_P) \quad \forall N \in Neighbors(P) \tag{8}$$

Control volume P and its neighboring volumes are illustrated in Fig. 2. j is some point within the control volume P, and R is the reconstruction operator given by:

$$R_P(\mathbf{r}_j) = \Phi_P + \Psi_j \nabla\Phi_P \cdot (\mathbf{r}_j - \mathbf{r}_P) \tag{9}$$

where Ψ is the flux limiter, and $\mathbf{r}$ is the position vector.

The idea of the reconstruction is to find the largest admissible Ψ while involving the monotonicity principle that values of the linearly reconstructed function must not exceed the maximum and minimum of neighboring centroid values. The computation of the flux limiter Ψ is performed in two steps as follows:

The reconstruction value is evaluated at each of the control volume's vertices in order to determine the flux limiter:

$$\Psi_j = \begin{cases} min\left(1, \frac{max(\Phi_N,\Phi_P)-\Phi_P}{\nabla\Phi_P\cdot(\mathbf{r}_j-\mathbf{r}_P)}\right), & \Phi_j > \Phi_P \\ min\left(1, \frac{max(\Phi_P-\Phi_N,\Phi_P)}{\nabla\Phi_P\cdot(\mathbf{r}_j-\mathbf{r}_P)}\right), & \Phi_j < \Phi_P \\ 1, & \Phi_j = \Phi_P \end{cases} \tag{10}$$

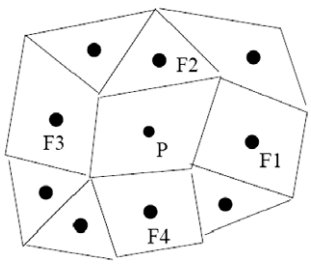

Fig. 2. Illustration of control volume P and its neighbors, F_1, F_2, F_3, F_4.

The value of the limiter is computed as the minimal values of Ψ_j over all vertices, i.e.

$$\Psi_P = min(\Psi_j) \tag{11}$$

such that during the linear reconstructions new extrema are not created and this scheme is equivalent to TVD–MUSCL scheme for a one-dimensional discretization.

A numerical experiment was performed on the classical Sod's shock tube problem. Solution was obtained on a two dimension 50×3 coarse mesh and the result was plotted against the exact Riemann solution in Fig. 3. Second order linear reconstruction and second order Runge–Kutta time integration were implemented in the scheme. Significant improvement on resolution was shown particularly on the density discontinuity as compared with first order upwind scheme discussed in Gong [4].

4. Numerical implementation

4.1. Centroid of control volume (face)

In the control volume approach, the conservative and primitive variables are located at the *centroid* of the face (the polygon which forms the control volume). As a convex face can be divided into triangles, the location of the centroid $\mathbf{r}_G$ can be expressed in terms of the centroid of the triangles:

$$\mathbf{r}_G = \frac{\sum_{i=1}^{N}(\mathbf{r}_{Gi} * S_i)}{\sum_{i=1}^{N} S_i} \tag{12}$$

where

N is the total number of triangles that form the convex polygon.

r_{Gi} is the centroid of each individual triangle and can be expressed as the algebraic average of the locations of the three vertices that forms that triangle:

$$\mathbf{r}_{Gi} = \frac{1}{3}(\mathbf{r}_i + \mathbf{r}_{i+1} + \mathbf{r}_{i+2}) \tag{13}$$

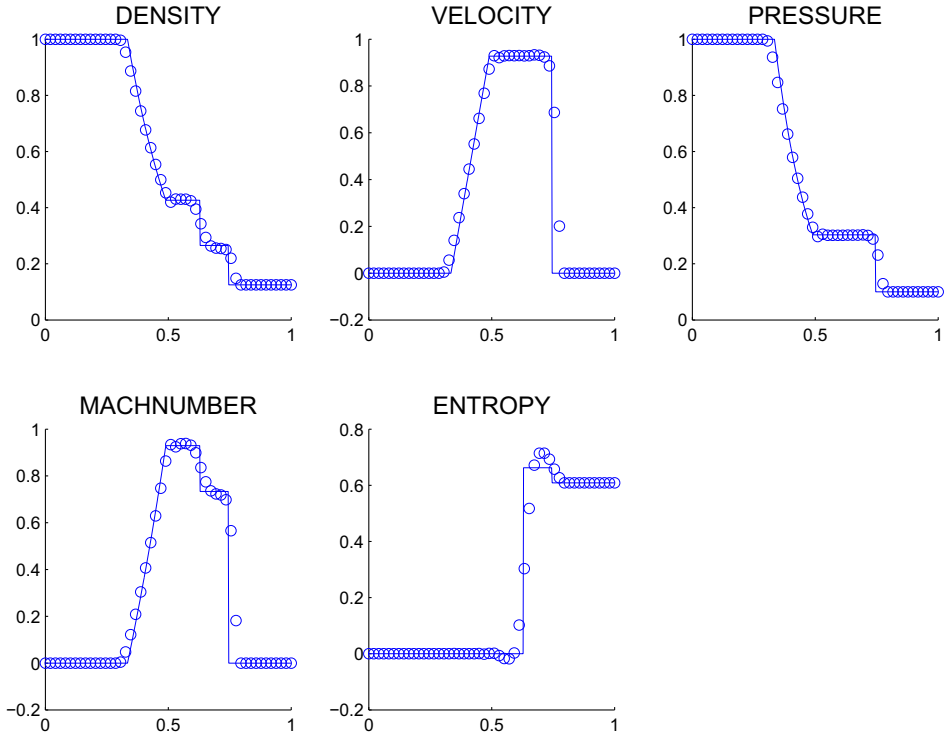

Fig. 3. Sod's shock tube problem: continuous line, exact solution; o solution with second order MUSCL projection and second order Runge–Kutta time stepping.

S_i is the area of the triangle, given by:

$$S_i = \frac{1}{2}|(\mathbf{r}_i - \mathbf{r}_{i+1}) \times (\mathbf{r}_i - \mathbf{r}_{i+2})| \tag{14}$$

4.2. Control volume lengths

When the algorithm is globally-explicit, the *CFL* condition must be met at all times and for all control volumes(faces) in the mesh(cell). Thus it becomes necessary to determine the lengths (or path) that the information must propagate to get through a specific volume. Previously, it was mentioned that all of the quantities were assumed to locate at the centroid of the face. Thus, the distance travelled by any information must be measured from the centroid to the current edge of the face we are considering. This distance should be measured in such a way that the length vector is normal to the edge of the face. In the *CFL* condition

$$CFL = \frac{\Delta t|\lambda_{max}|}{\Delta x}, \tag{15}$$

this length vector can be referred to as Δx, or the spacing of the grid points where Δt and λ_{max} are respectively the time step and the maximum wave speed travelling through the face.

This length must be measured for all of the edges in the cell. Note that each edge has two related distances, corresponding to the two faces that share this particular edge and so $\Delta x = \Delta x^L + \Delta x^R$ where L and R refer to the corresponding lengths of the left and right faces of a given edge.

4.3. Evaluation of gradient

Face gradients are required to evaluate the viscous terms in the Navier–Stokes equations as well as to contract the high order upwind schemes.

One approach to get the gradients consists of first computing the gradients at the mesh vertices and then averaging these to the interfaces Frink [39]. Such kind of discretization can also be derived by using a Galerkin finite element procedure and assuming linear variation of the flow variables on the interfaces Mavriplis [40]. There are also schemes constructed by using Green–Gauss integration, and this method was later extended as the least-squares technique, which was shown to yield good approximations on distorted meshes Barth [37].

Least-square method is also referred to as the minimum energy reconstruction. It simply consists of fitting a linear function to the value of the neighboring nodes using the least-square technique. This is well documented in Sun [41].

Suppose we are seeking the gradient $\nabla\xi = (\xi_x, \xi_y, \xi_z)$ of a scalar function ξ at node i. Values ξ_i and ξ_j at node i and its neighboring nodes j are known. The gradient is estimated by minimizing the distance between ξ_j and a piecewise approximation

$$\xi_{j'} = \xi_i + \nabla\xi \cdot \Delta\mathbf{r}_{ji}, \tag{16}$$

where $\nabla\mathbf{r}_{ji} = (\Delta x_{ji}, \Delta y_{ji}, \Delta z_{ji}) = (x_j - x_i, y_j - y_i, z_j - z_i)$. The distance is expressed as

$$\sum_j (\xi_j - \xi_{j'})^2 = \sum_j |\xi_j - (\xi_i + \nabla\xi \cdot \Delta\mathbf{r}_{ji})|^2 \tag{17}$$

where $\sum_j$ represents summing all neighboring nodes of node i. Minimizing the distance leads to a linear system,

$$\begin{matrix}
\left(\sum_j \Delta x_{ji}\Delta x_{ji}\right)\xi_x & \left(\sum_j \Delta x_{ji}\Delta y_{ji}\right)\xi_y & \left(\sum_j \Delta x_{ji}\Delta z_{ji}\right)\xi_z & \sum_j \Delta x_{ji}\Delta\xi_{ji} \\
\left(\sum_j^j \Delta y_{ji}\Delta x_{ji}\right)\xi_x & \left(\sum_j^j \Delta y_{ji}\Delta y_{ji}\right)\xi_y & \left(\sum_j^j \Delta y_{ji}\Delta z_{ji}\right)\xi_z & \sum_j^j \Delta y_{ji}\Delta\xi_{ji} \\
\left(\sum_j^j \Delta z_{ji}\Delta x_{ji}\right)\xi_x & \left(\sum_j^j \Delta z_{ji}\Delta y_{ji}\right)\xi_y & \left(\sum_j^j \Delta z_{ji}\Delta z_{ji}\right)\xi_z & \sum_j^j \Delta z_{ji}\Delta\xi_{ji}
\end{matrix} \tag{18}$$

or, simply

$$\mathbf{A}\mathbf{x} = \mathbf{b} \tag{19}$$

where $\mathbf{A}$ is a matrix of the coefficients obtained from the left hand side of Eq. (18), $\mathbf{b}$ represents the right hand side of the equation, and $\mathbf{x} = (\xi_x, \xi_y, \xi_z)^T$. Then we have

$$\mathbf{x} = \mathbf{A}^{-1}\mathbf{b} \tag{20}$$

5. Data structure

5.1. Data structure for numerical simulation

Discretization techniques for partial differential equations come with a large varieties of different data structures. Not only must represent the conservation variables themselves for each control volume, but must also represent the connectivity or topological relationships between the control volumes for the calculation of convective fluxes. Generally, data structures can be summarized into two categories, the *edge-based* and the *element-based* data structures.

Traditionally, finite element methods (FEM) used in structural analysis have relied on element-based data structures, where for each element of the mesh a list of the forming vertex addresses is stored. Typically, cell types are restricted to one or a few fundamental convex polytopes, like triangles or quadrangles in 2D and tetrahedrons, prisms or cubes in 3D.

However, unlike the FEM problem, finite volume methods (FVM) are less restrictive on the type of cells so edge-based data structure is necessary. A natural type of data structure is the structured mesh, i.e. array-based data structure. Such array-based data structures store the subdivision connectivity of each control facet as a 2D array. Since the adjacency relations of the array are implicit they need not be maintained. While such kind of control volumes allow a straightforward and efficient implementation of computational algorithms for general problems, their application to complex geometries and adaptive mesh refinement requires a substantial amount of effort.

This limitation can be lifted by the implementation of an unstructured mesh. However, as there is no rigid connectivity rules at the vertices, no implicit array-based data structure exists. Consequently, unstructured FVM are typically implemented using an edge-based data structure Mavriplis [42], either cell-centered or cell-vertex oriented. The cell-centered data structure consist of a list of cells, each with references to its vertices and cell-neighbors. The corresponding conservation variables are stored at the centroid of the cells. In the cell-vertex approach the grid is stored following grid nodes or vertices and the variables are stored at the vertices. Although no conservative variables are stored on the edge, the change of the conservative values in a cell is equal to the sum of fluxes through its interfaces, i.e. the dual edges that join two neighboring cell centroids and pierces the face common to these two cells in the vertex-based scheme or the edges which connect two adjacent vertices in that cell for the cell-centered scheme.

While an edge-based data structure is a necessity for maintaining of connectivity or topological relationships between the control volumes, it also has its disadvantages. It requires a preprocessing operation to extract a unique list of edges from the list of mesh elements and to compute the associated edge coefficients Mavriplis [42]. For unsteady flows with dynamic meshes, this preprocessing must be performed every time the mesh is altered, although this may be done locally. Additionally, for dynamic grid cases, element based data structures are generally required for performing mesh motion or adaptation, since edge lists represent a lower-level description of the mesh.

This shortcoming was over came by Sun [41], who proposed an essentially vectorizable cell-face data structure for any unstructured quadrilateral and hexahedral grids. The data structure is a bi-directional reference between cell and face with a strict ordering method, which is based on the *Königsberg bridge* problem. However, the dynamic grid refinement is confined to simple topological changes in this method.

5.2. Quad-edge data structure

The aforementioned restrictions can be eliminated by the implementation of the *quad-edge* data structure of Quibas and Stolfi [25]. Other commonly used data structures used in computational geometry are: *winged-edge* of Baumgart [43], *split-edge* [44] and the *lath-based* [45] data structure. The incidence queries offered by these implementations rely on the ordering of edges around faces and vertices, and access to the next and previous edges at both vertices are explicitly given. All these data structures also support modifying operations. They offer some variants of Euler operators, such as attaching, splitting and deleting cells, while generally the data structure used in numerical simulation only allow refinement and derefinement operations Berti [46].The uniqueness of the *quad-edge* data structure is its duality, with which vertices and faces are treated similarly. It is not only useful in the sense of Voronoi diagrams and Delaunay triangulation, but it also facilitates the search of vertices/edges/faces immediately adjacent to a given vertex/edge/face in constant time. With such duality, element-based data structures are no longer needed for nonsimplicial computation stencils.

The quad-edge data structure implementation was adapted from Paul Heckbert at CMU [47]. This data structure is originally written for describing the topology and geometry of polyhedra in computational geometries. It offers excellent adjacency queries efficiency and elegant Euler operation over the mesh, which make it very promising in the numerical simulation area, where the finite volume method requires effective methods in neighbor querying and mesh adaption. It can also deal with arbitrary polygonal unstructured control volumes. Number of sides per control volume severely interferes with the mesh regeneration process due to mesh moving and local refinements are no longer restricted.

In the *quad-edge* data structure, there are classes for vertices, edges, and faces, but edges play the leading role. The edges store complete topological information; all of the topological information stored by the faces and vertices is redundant with information in the edges. Figuratively speaking, the edges form the skeleton, and the vertices and faces are optional decorations, hanging off of the edges. Vertices hold most of the geometric (shape) information. Further details of the data structure are described in Gong [4].

6. Adaptive mesh refinement

Adaptive mesh refinement techniques which automatically adapt the computational grid to the solution of the governing partial differential equations can be very effective in improving solution accuracy or treating problems with disparate length scales. It has progressed rapidly over the last decade and the main types of optimal mesh criteria, error indicators/estimators and refinement strategies were reviewed and compared by Lohner [48]. There are two motivations for using adaptive mesh refinement.

- With mesh adaption, the numerical solution to a specific problem can be achieved with the least number of degree of freedom which yields less amount of work for a given accuracy.
- Physical phenomena have disparate length scales and thus if the grid is allowed to adapt to the solution, users no longer waste time choosing a grid that is suitable for the problem at hand. It is of more importance for transient problems with travelling discontinuities such as shocks and contact surfaces. In this way, such regions of our interest will be studied with high resolution.

6.1. Mesh refinement indicator

To design an adaptive mesh procedure, a quantitative assessment of the optimality of the adaptive mesh procedure is required. Such criterion can be based on the geometry of the simulation domain or the physical phenomena. A criterion adopted in the current study is to refine the mesh such that the numerical error is distributed equally in the computational domain, where mesh refinement will be applied to those cells in which error is large. Two different error indicators are tried in the current numerical experiments.

One error indicator is based on the jumps of indicator variables. This error indicator implicitly assumes first order accuracy for the underlying scheme so the preliminary numerical result in the current numerical application is not optimal as second order numerical scheme was used in the current research.

The second error indicator is to compare different orders of derivatives. The underlying assumption is that the solution should be smooth at the order of desired numerical accuracy, i.e. the difference between Taylor series expansion on flow variables of higher order and that of desired order should be minimized with localized mesh refinement.

Mesh refinement indicator also has to be non-dimensionalized such that it will be able to indicate strong flow features (e.g. strong shocks) and weak features (secondary shocks, contact discontinuities) as well. Such indicator was proposed in Lonher [49]. In general terms, it is of the form

$$error = \frac{h^2|seconddederivatives|}{h|firstderivatives| + \alpha_f|meanvalue|} \tag{21}$$

By dividing the second derivatives by the absolute value of the first derivatives, the error indicator becomes bounded, dimensionless and the "eating up" effect of strong features is avoided. The terms following α_f are added as a noise filter in order not to refine wiggles or ripples which may appear due to loss of monotonicity.

The current criterion for adaption is:

$$\varepsilon_T = Max\left(\frac{|(\nabla_{l\rho})_C - (\nabla_{l\rho})_i|}{\alpha_f\rho_c/dl + |(\nabla_{l\rho})_i|}, \frac{|(\nabla_{l\rho})_C - (\nabla_{l\rho})_j|}{\alpha_f\rho_c/dl + |(\nabla_{l\rho})_j|}\right) \tag{22}$$

where ε_T is the truncation error indicator, as shown in Fig. 4(a), i,j are indices of two neighboring cells, ∇_l is the gradient along the lines connecting two neighboring cells, index C denotes the center of the edge that cell i and j share. α_f is the noise filter, typical value is 0.03. dl is the distance between two neighboring cells' centroid. For each cell, ε_T was evaluated at all of its interfaces and the cell will be:

- refined if maximum of ε_T of all neighboring edges $> \varepsilon_r$;
- coarsen if maximum of ε_T of all neighboring edges $< \varepsilon_c$.

ε_r and ε_c are two threshold values for refinement and coarsening with typical values: $\varepsilon_c = 0.05$ and $\varepsilon_r = 0.08$.

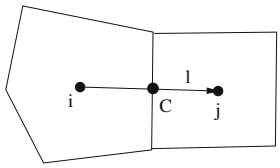

Fig. 4(a). Sketch of the cell interface between neighboring cells i and j.

6.2. Mesh refinement strategies

Mesh refinement strategies are referring to how the mesh is divided or merged and geometrical topology information is updated during the adaption process. A classical *h-refinement* method was chosen such that cells are subdivided by four where higher mesh densities were needed. The process of refinement and coarsening was illustrated in Fig. 4(b) accomplished with basic Euler operation facilitated by the *quad-edge* mesh data structure such that geometrical topology information of each cell and corresponding vertices, edges was updated within the quad-edge class. Recursive subdivision and agglomeration are achieved through two refinement level indicators: cell adaption level and vertices adaption level. As geometrical topology information is updated locally, such implementation is highly efficient and coding can be unified for cell flux evaluation, refined cells were treated the same way as coarsen cells.

6.3. Numerical experiment

A test case was carried out to evaluate the effectiveness of the current adaptive mesh refinement procedure. A supersonic flow over a ramp was simulated with the inlet boundary at left set as $M = 1.5, P = 1$. The initial coarse mesh used for the calculation was shown in Fig. 5(a). Computation was performed with two levels of adaptive mesh refinement and ended at time $t = 2.0$. Fig. 5(b) shows the final refined mesh. Fig. 5(c) shows the pressure contour plotted on the refined mesh. Mesh was effectively refined at the flow discontinuity and a significant improvement on the resolution of the shock wave was observed.

7. Treatment of moving boundary

7.1. Closely coupled model of fluid structure interaction

The prediction of fluid and structure interaction phenomena requires solving simultaneously the coupled fluid and structural equations of equilibrium. In this process, a closely coupled model is one of the most widely used methods in the field of

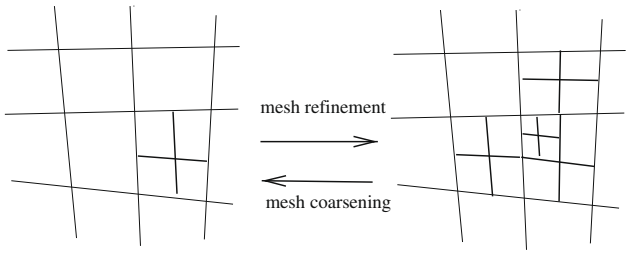

Fig. 4(b). Illustration of adaptive mesh refinement strategy.

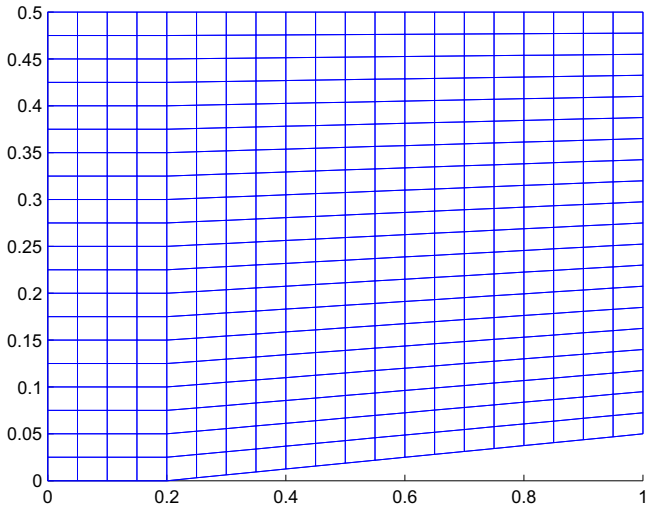

Fig. 5(a). Initial coarse mesh used for supersonic flow passing a ramp.

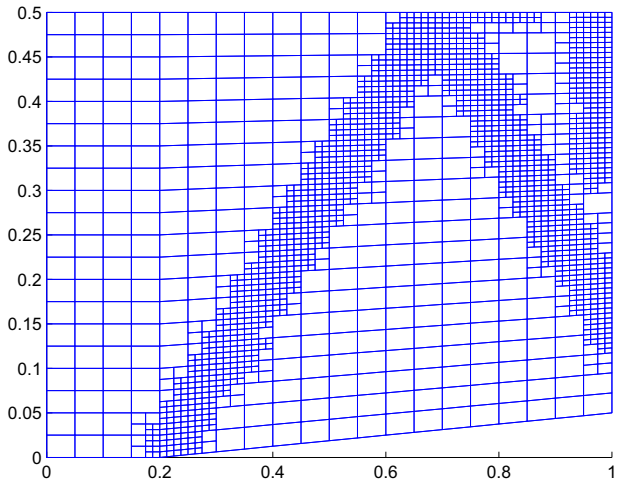

Fig. 5(b). Refined mesh for supersonic flow passing a ramp, at $t = 2$.

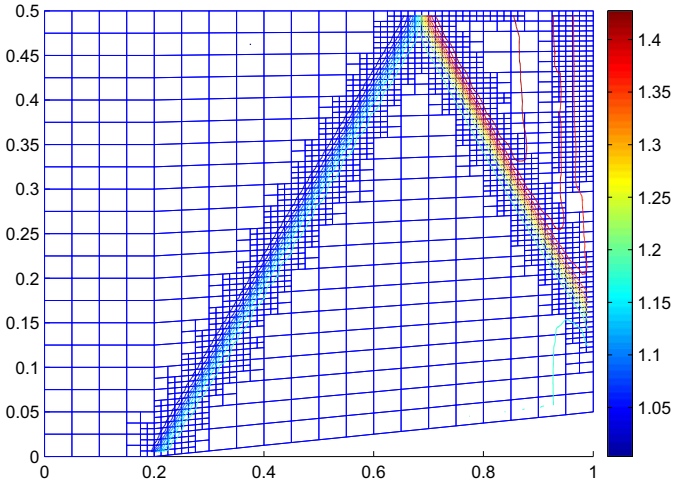

Fig. 5(c). Pressure contour on refined mesh for supersonic flow passing a ramp, at $t = 2$.

CAE as it not only paves way for the use of different solvers for fluid and structure models, but also couples the solvers in a tight fashion thereby making it an efficient method for complex non-linear problems [16]. The fluid and structure equations are solved separately in this CAE approach using different solvers but are coupled into one single module with information being exchanged at the interface or the boundary via an interface module thereby making the entire CAE model tightly coupled. The information exchanged at this interface includes the surface loads, which are mapped from CFD surface grid onto the structure dynamics grid; and the displacement field, which are mapped from structure dynamics grid onto CFD surface grid. The transfer of surface displacement back to the CFD module implies deformation of the CFD surface mesh and this calls for a moving boundary technique to enable re-meshing the entire CFD domain as we march in time.

The current implementation is of first order in accuracy and is depicted in Fig. 6(a). At every time step on the interface boundary, load is transferred to the structure from fluid as a pressure loading on the structural element and the motion of the structure is transferred to the fluid domain by dynamically updating the computational mesh.

7.2. Mesh adjustment on moving boundary

To transfer the structural motion back to the fluid domain during the numerical simulation of coupled fluid–structure interaction, various methods have been developed in the past, including the cartesian cut-cell methods developed by De Zeeuw and Powell [17], overset mesh [18], arbitrary Lagrangian–Eulerian (ALE) methods [19], the interface tracking methods of Glimm et al. [20], immersed boundary methods [21] and recently the external force method [22].

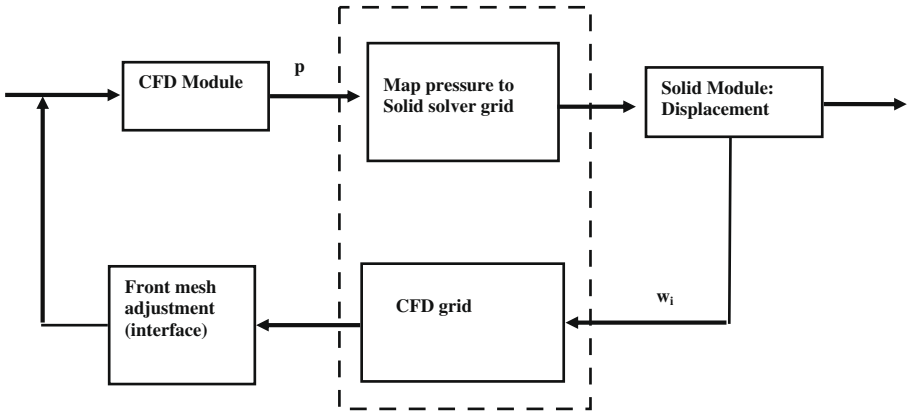

Fig. 6(a). Block diagram of coupling between solid and fluid solvers.

Some methods require a mesh topology change during the treatment of moving boundaries. Two popular approaches are, mesh regeneration at the moving boundary or deformation of the computational mesh to accommodate the interface motion.

Popular ALE methods involve deforming mesh which may result in poor mesh quality and generally it requires the interpolation of flow variables, while such interpolation processes are not conservative, though they can be accurate and reliable in some cases [23]. However, the advancing front approach addresses the moving grid problem in a way that the interpolation process is circumvented. Mesh is locally regenerated on the moving boundary at each computation step and internal mesh interfaces are not changed, such that no interpolation of velocity is involved in the flux calculation. Such schemes maintain a conservation on all conservative flow variables while optimal mesh quality is also achieved.

This advancing front method is implemented to avoid high aspect-ratio or highly skewed cells. To avoid cutting cells that are a small fraction of the size of uncut cells, such a cell is merged with neighboring uncut cells if necessary. These implementations result in smooth high quality mesh in most regions of the flow field.

Again the process of advancing front mesh regeneration was greatly benefited by the implementation of *quad-edge* data structure [25]. Efficient algorithms were made possible for the mesh splitting and agglomerating. When an individual element was added to the boundary one at a time at an existing front, mesh topology was updated inherently during the basic mesh Euler operation such that time consuming global iteration was not needed.

When new mesh is generated by the subdivision algorithm, additional vertices are inserted into the mesh. During the mesh simplification process, some vertices may be deleted. Such newly generated or deleted vertices generally result in faces with an arbitrary number of edges. The current numerical code was implemented in a way such that faces with an arbitrary number of edges were treated normally in computation.

Several features of the control volume splitting and merging process are illustrated in Figs. 6(b) and 6(c). As a result of the structure boundary moving towards the flow region, edges of the corresponding boundary control volume may fall short of the predefined critical length, such boundary control volumes will be merged with its immediate inner control volume. However, such inner control volume may have been refined during the adaptive mesh refinement process so it will be coarsen first. A recursive algorithm is implemented such that the level of refinement would return to its original status of one. After the coarsening process, the edge shared by these two control volumes is deleted and corresponding vertices may also be deleted if the neighboring control volume has also been merged. Corresponding conservative variables are summed up for those merging control volumes and new primitive values are updated as well as the corresponding geometry variables such as the edge length, control volume centroid and area. The splitting of a control volume was relatively more straightforward. New vertices were inserted in the middle of the corresponding edge if necessary and a new edge would be created linking these vertices, which would split the control volume in half. The newly created control volume has its conservative variables

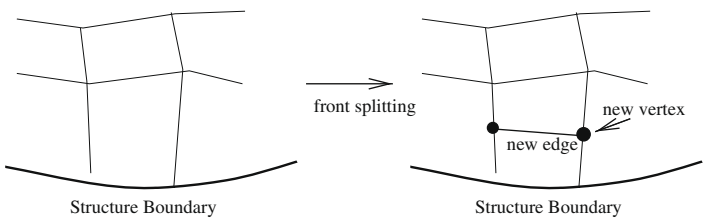

Fig. 6(b). Illustration of control volume splitting during the advancing front mesh adjustment.

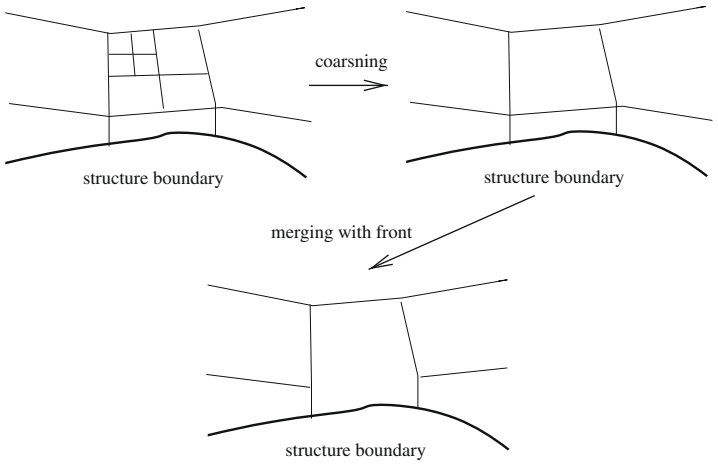

Fig. 6(c). Illustration of control volume merging during the advancing front mesh adjustment.

interpolated and subtracted from the original control volume. Geometry variables were updated as well correspondingly. As there are no intergradation of primitive variables and no inner edge movement involved in such implementation, this method is fully conservative.

7.3. A numerical flux evaluation on adjusted mesh

Traditional ALE methods were implemented as in [19]:

$$\frac{\mathrm{d}}{\mathrm{d}t}\int_V \rho\,\mathrm{d}V - \int_S \rho(U-u)\cdot n\,\mathrm{d}S = 0 \tag{23a}$$

$$\frac{\mathrm{d}}{\mathrm{d}t}\int_V \rho u\,\mathrm{d}V - \int_S \rho u(U-u)\cdot n\,\mathrm{d}S + \int_V \nabla p\,\mathrm{d}V - \int_V \rho g\,\mathrm{d}V = 0 \tag{23b}$$

$$\frac{\mathrm{d}}{\mathrm{d}t}\int_V \rho E\,\mathrm{d}V - \int_S \rho E(U-u)\cdot n\,\mathrm{d}S + \int_S \nabla p u\cdot n\,\mathrm{d}S - \int_V \rho g\cdot u\,\mathrm{d}V = 0 \tag{23c}$$

In these expressions $\mathbf{U}$ is the velocity of the surface S. When $\mathbf{U}=0$ the equations are Eulerian, and when $\mathbf{U}=\mathbf{u}$ the equations are Lagrangian. If the control volume is under displacement and expansion/deformation at the same time, the velocity on the surface of the control volume will be a combination of the control volume centroid velocity and a term related to its expansion/deformation rate, $\mathbf{U}=\mathrm{d}r/\mathrm{d}t+\mathrm{d}\mathbf{u}/\mathrm{d}r\cdot dl$ as shown in Fig. 7(a). If the mesh is under global movement, $\mathbf{U}$ is not zero everywhere such that it has to be accounted for on each control volume surface, and furthermore, $\mathbf{u}$ will have to be interpolated under a new mesh topology and it may affect the flow solver's accuracy and stability. Under the proposed advancing front method, as shown in Fig. 7(b), we have $\mathbf{U}=0$ on all internal control volume surfaces and $\mathbf{U}=\mathbf{u}$ on structure boundary. Consequently in Eq. (23a) surface integral on conservative variable $\mathbf{w}$, $\int_S \mathbf{w}(\mathbf{U}-\mathbf{u})\cdot\mathbf{n}\,\mathrm{d}S$ is 0 and no interpolation velocity will be directly involved in the flux calculation. Under a second order MUSCL scheme, primitive variables maybe needed for the Riemann solver and the velocity on the boundary control volume centroid can be calculated directly from updated conservative variables as well as the new geometrical variables including new centroid position and control volume area.

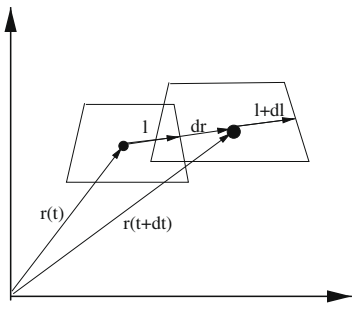

Fig. 7(a). Illustration of ALE control volume.

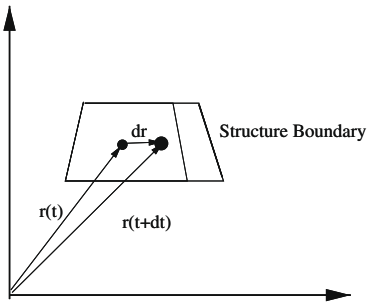

Fig. 7(b). Illustration of advancing front.

7.4. Numerical experiment

Numerical experiments were carried out to confirm the effectiveness of the current advancing mesh approach. Fig. 8(a) shows the mesh with initial adapt mesh refinement used for numerical simulation. The lower boundary is the structure boundary so during the simulation, it will deform when aerodynamic loading is applied; as a result, new mesh is generated next to the structure boundary as illustrated in Fig. 8(b). As the structure boundary started moving towards the inner flow region, the inner mesh is automatically removed as shown in Fig. 8(c). Such mesh regeneration process is performed at each simulation time step and all boundary control volumes are automatically adjusted according to their corresponding boundary position. One level of adaptive mesh refinement is also performed within each time step so density discontinuities such as contact surface can be resolved with high resolution.

8. Finite element solver: axisymmetric shell model

The problem of a circular plate under shock wave loading is modelled with a finite element axisymmetric shell model as in [24]. Using the Kirchhoff–Love assumption, the problem is greatly simplified and the element is essentially 'one-dimensional'.

The four strain components are given by:

$$\boldsymbol{\varepsilon} = \begin{Bmatrix} \varepsilon_s \\ \varepsilon_\theta \\ \chi_s \\ \chi_\theta \end{Bmatrix} = \begin{Bmatrix} \mathrm{d}\bar{u}/\mathrm{d}s \\ (\bar{u}cos\phi - \bar{w}sin\phi)/r \\ -\mathrm{d}^2\bar{w}/\mathrm{d}s^2 \\ -(\mathrm{d}\bar{w}/\mathrm{d}s)cos\phi/r \end{Bmatrix} \tag{24}$$

The four internal stress are related to the strains by an elasticity matrix **D**:

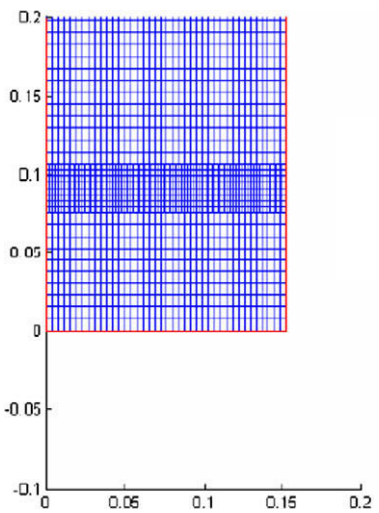

Fig. 8(a). Initial mesh after first step of adapt mesh refinement.

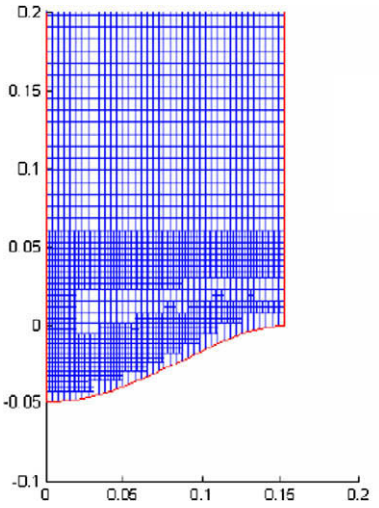

Fig. 8(b). Mesh at = 0.00383 with advancing front on structure boundary.

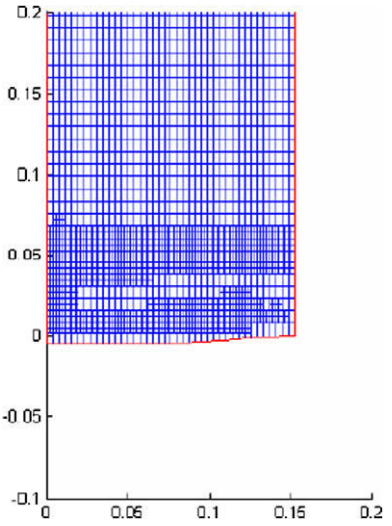

Fig. 8(c). Mesh at = 0.00555 with advancing front on structure boundary.

$$\boldsymbol{\sigma} = \begin{Bmatrix} N_s \\ N_\theta \\ M_s \\ M_\theta \end{Bmatrix} = \mathbf{D}\boldsymbol{\varepsilon} \tag{25}$$

which for an isotropic shell becomes:

$$\mathbf{D} = \frac{Et}{1-\nu^2}\begin{bmatrix} 1 & \nu & 0 & 0 \\ \nu & 1 & 0 & 0 \\ 0 & 0 & t^2/12 & \nu t^2/12 \\ 0 & 0 & \nu t^2/12 & t^2/12 \end{bmatrix} \tag{26}$$

where E and ν are the Young's modulus and Poisson's ratio, t is the thickness of the shell.

The displacements of a point on the middle surface of the element, $\bar{u}$ and $\bar{w}$ in the local coordinate, can be expressed by its position within the element, s and the coefficients $a_1, a_2, \ldots, a_6$ which satisfy slope and displacement continuity. Solving the equations for $a_1, a_2, \ldots, a_6$ the following equation can be obtained for $\bar{u}$ and $\bar{w}$:

$$\bar{\mathbf{u}} = \begin{Bmatrix} \bar{u} \\ \bar{w} \end{Bmatrix} = \overline{N}\mathbf{a}^{\mathbf{e}} \tag{27}$$

where

$$\overline{N} = [\overline{N}_1, \overline{N}_2] \tag{28}$$

$$\overline{N}_1 = \begin{bmatrix} \frac{1}{2} - \frac{1}{2}\xi & 0 & 0 \\ 0 & \frac{1}{2} - \frac{3}{4}\xi + \frac{1}{4}\xi^3 & \frac{1}{8}L(1 - \xi - \xi^2 + \xi^3) \end{bmatrix} \tag{29}$$

$$\overline{N}_2 = \begin{bmatrix} \frac{1}{2} + \frac{1}{2}\xi & 0 & 0 \\ 0 & \frac{1}{2} + \frac{3}{4}\xi - \frac{1}{4}\xi^3 & \frac{1}{8}L(-1 - \xi + \xi^2 + \xi^3) \end{bmatrix} \tag{30}$$

where $\xi = 2s/L - 1$.

At the node i we have the following relationship between local and global coordinate:

$$\begin{Bmatrix} \bar{u}_i \\ \bar{w}_i \\ (\mathrm{d}\bar{w}/\mathrm{d}s)_i \end{Bmatrix} = \begin{bmatrix} cos\phi & sin\phi & 0 \\ -sin\phi & cos\phi & 0 \\ 0 & 0 & 0 \end{bmatrix} = \begin{Bmatrix} u_i \\ w_i \\ \beta_i \end{Bmatrix} = \mathbf{T}\mathbf{a}_i \tag{31}$$

such that the global interpolation is

$$\mathbf{u} = \begin{Bmatrix} u \\ w \end{Bmatrix} = [\overline{N}_1\mathbf{T} \quad \overline{N}_2\mathbf{T}]\mathbf{a}^{\mathbf{e}} = N\mathbf{a}^{\mathbf{e}} \tag{32}$$

We can obtain the strain matrix $\mathbf{B}$ by using equation:

$$\boldsymbol{\varepsilon} = [\overline{B}_1\mathbf{T}, \overline{B}_2\mathbf{T}]\mathbf{a}^{\mathbf{e}} = B\mathbf{a}^{\mathbf{e}} \tag{33}$$

where

$$\overline{B}_1 = \begin{bmatrix} -L^{-1} & 0 & 0 \\ -\frac{1}{2}\frac{-1+\xi}{r}sin\phi & \left(\frac{1}{2} - \frac{3}{4}\xi + \frac{1}{4}\xi^3\right)\frac{cos\phi}{r} & \frac{1}{8}L(1 - \xi - \xi^2 + \xi^3)\frac{cos\phi}{r} \\ 0 & -6\frac{\xi}{L^2} & -\frac{-1+3\xi}{L} \\ 0 & -\frac{3}{2}\frac{-1+\xi^2}{rL}sin\phi & -\frac{1}{4}\frac{-1-2\xi+3\xi^2}{r}sin\phi \end{bmatrix} \tag{34}$$

$$\overline{B}_2 = \begin{bmatrix} L^{-1} & 0 & 0 \\ \frac{1}{2}\frac{1+\xi}{r}sin\phi & \left(\frac{1}{2} + \frac{3}{4}\xi - \frac{1}{4}\xi^3\right)\frac{cos\phi}{r} & \frac{1}{8}L(-1 - \xi + \xi^2 + \xi^3)\frac{cos\phi}{r} \\ 0 & 6\frac{\xi}{L^2} & -\frac{1+3\xi}{L} \\ 0 & \frac{3}{2}\frac{-1+\xi^2}{rL}sin\phi & -\frac{1}{4}\frac{-1+2\xi+3\xi^2}{r}sin\phi \end{bmatrix} \tag{35}$$

The stiffness matrix in local coordinates:

$$\overline{K} = \int_{-1}^{1} \overline{B}^T\mathbf{D}\overline{B}\pi rL\,\mathrm{d}\xi \tag{36}$$

On transformation, the stiffness matrix K on the global matrix is given by

$$K = \mathbf{T}^{\mathbf{T}}\overline{K}\mathbf{T} \tag{37}$$

The corresponding nodal load from distributed load q on the element is evaluated as:

$$Q_i = T^T \int_{-1}^{1} \overline{N}_i^T q\pi rL\,\mathrm{d}\xi \tag{38}$$

In this work the above integration is evaluated numerically on the Gauss points of the element.

9. Newmark integration method

The time integration scheme for the dynamic structural FEM modal in coupled fluid–structural simulation has been reviewed and discussed in [16]. There are several ways to integrate the modal equations of motion. The schemes range from explicit central difference schemes to implicit schemes such as the Houbolt, Wilson-y and Newmark methods [25,26]. The explicit scheme was found to be conditionally stable as limited by the choice of time step size. Therefore one may be forced to perform iterations of the structure solver to synchronize with the time step of the implicit flow solver. Implicit time integration schemes are unconditionally stable and among them, the classical Newmark algorithm is one of the most popular for dynamic analysis. It has been proven that the Newmark method performs best for $Dt/T < 0.01$; where T is the time period of

vibrations and hence time step size must be chosen appropriately to obtain best accuracy. On the consideration of accuracy and stability, we choose the Newmark scheme as the time integration scheme for the structural equations of motion.

The FEM program was coded in C++ and was validated by comparing with other known solutions under both cases of static and dynamic loading.

The analytical solution of an axisymmetric plate under distributed static load can be found in [27]. If a circular plate of radius a carries a load of intensity q uniformly distributed over the entire surface of the plate, and if the plate is clamped along its edge, then the deflection of the plate w is:

$$w = \frac{q}{64D}(a^2 - r^2)^2 \tag{39}$$

This solution is plotted along with the FEM numerical solution in Fig. 9(a). The parameters used in the present numerical solution are:

$$\begin{aligned} a &= 10\ \text{m} \\ h &= 1\ \text{m} \\ E &= 1000\ \text{Pa} \\ v &= 0.33 \\ D &= \frac{Eh^3}{12(1-v^2)} = 93.5174\ \text{N m} \\ q &= 0.0318 \end{aligned} \tag{40}$$

Twenty elements were used in this simulation and good agreement was found between the FEM solution and analytical solution.

To validate the dynamic model of current FEM code, the problem of an aluminum circular plate fully clamped around its outer boundary and subjected to transverse impulse loading was used as a test case. Such a problem was analyzed in the past and though various analytical solutions exist, for simplicity, the current result was compared with the LS-DYNA numerical solution. The parameters used for this test are those in Case #1 with the aluminum plate with additional force, $f = 444.8$ N.

A comparison of center transverse deformation between the two numerical solutions is shown in Fig. 9(b). A discrepancy of 10% that is observed in the comparison may have been caused by the use of triangular shell elements in the LS-DYNA model which may resulted in extra stiffness. Note that LS-DYNA result was obtained by using a central difference time integration scheme with a time step of about 5 μs and in the current FEM code, Newmark integration scheme was used with a time step of 20 μs. The modal frequency of the present FEM code is closer to the analytical solution of G&A.

It is also important to mention that since the Newmark scheme performs best for $Dt/T < 0.01$, very small time step is needed to fully resolve the high frequency modes. Under the current time step of 20 μs, first modes are fully resolved but significant discrepancy (20–30%) was observed for higher frequency modes. With the current closely coupled fluid–structure interaction scheme, the difficulty of resolving high frequency modes is that if the small time step is optimized for the structure solver, numerical dissipation will rise significantly in the fluid solver. However, as the goal of the current research is concentrated on the flow phenomena in the fluid–structure interaction process, the time step determined by the CFL condition of the flow solver will be used in the coupled solver. Also under the current configuration, experimental and analytical results both show that the amplitude of the first modes is of an order or more higher than that of the second modes so such compromise of time stepping is not expected to affect the flow phenomena significantly.

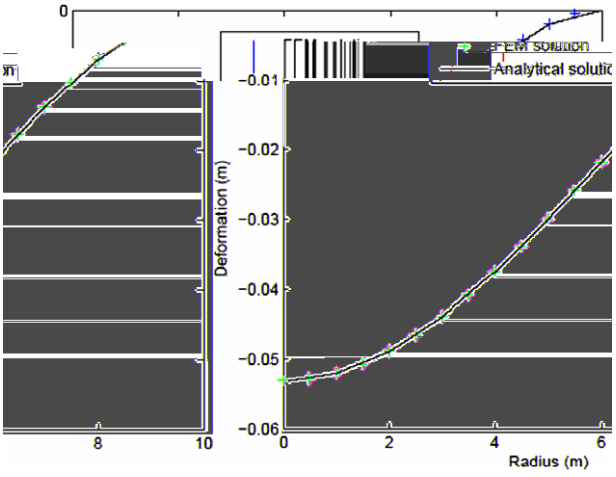

Fig. 9(a). Comparison of static and analytic solutions.

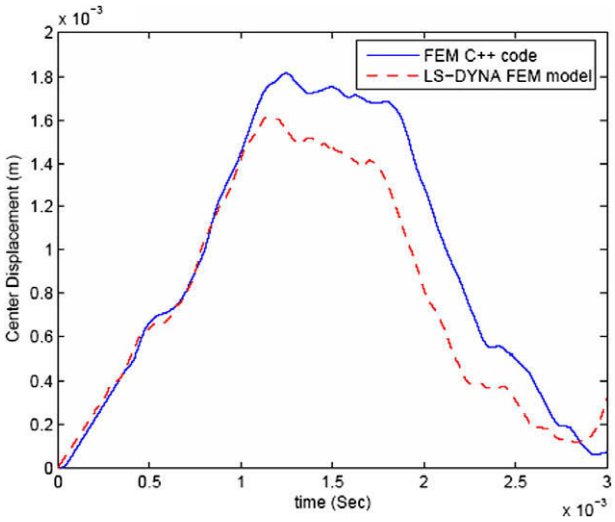

Fig. 9(b). Comparison of dynamic FEM and LS-DYNA results.

10. Results

10.1. Interaction of a planar shock wave and clamped circular aluminum plate

The flow field with a radius of 0.1524 m and height of 0.3048 m was discretized by 40×40 control volumes. The aluminum plate consists of 40 axisymmetric elements, with material properties corresponding to Case #1 shown in Table 1.

The flow field is initialized as:

$$\begin{cases} p = 2e5,\ \rho = 2.4,\ u = 0,\ v = 0 & \text{upper-region}: \ y > 0.1; \\ p = 1e5,\ \rho = 1.2,\ u = 0,\ v = 0 & \text{lower-region}: \ y < 0.1. \end{cases} \tag{41}$$

Given the initial condition, this is virtually a mini shock tube problem. It only differs in that the high pressure section is infinitely long such that all waves will be propagating though the open end. No adaptive mesh refinement was performed during this simulation and CFL number was chosen to be 0.95. Fig. 10 shows the meshes at different simulation time steps. Figs. 11 and 12 show the pressure contours of the flow field at different times.

Fig. 11(a) shows the initial condition, with which a shock wave is created that will be propagating towards the plate (negative y direction). The sudden motion of the shock wave generates also a set of expansion waves propagating in the opposite direction, i.e. towards the positive y direction which will lower the pressure along their path. Fig. 11(b) shows the pressure contour shortly after the shock wave has been reflected off the plate. No visible deformation was observed on the shock wave. However, there are weak expansion waves which follow immediately behind the shock. It is also shown that there are expansion waves emitting around the circle near the half radius of the plate, which appears to be excited by high order modes of the plate motion. Fig. 11(c) and (d) show the reflected shock wave continues propagating upwards and the flow field to be further affected by the waves generated as a result of the plate's transverse motion towards the negative y direction. It can also be noticed that as the plate starts to decelerate, it generates compression waves propagating into the flow field. After the plate reaches its maximum displacement and starts to accelerate upwards, further pressure build up in the flow field can be observed as in Fig. 11(e) and (f). The second cycle of the interaction is shown in Fig. 12, where expansion waves and compression waves can be observed repeatedly propagating from the surface of the plate into the flow field.

Fig. 13(a) shows the pressure history at the center of the plate together with that of a shock wave reflected off a rigid wall. The pressure reflected off the elastic plate fluctuates with a peak to peak magnitude of about 4000 Pa, equivalent to about 0.6 psi which represents a 2% variation of the initial pressure of 2×10^5 Pa. Such pressure fluctuation is related to the vibration of the plate and this dominant frequency appears to be the same as the first modal frequency of the plate. It is also evident that the magnitude of the pressure fluctuations decreases in time, while the center transverse displacement also

Table 1
Computed interactions: plate dimensions and material properties.

Plate	Plate material	Thickness h (mm)	Diameter α (mm)	Young's modulus E (GPa)	Poisson's ratio ν	Density kg/m^3 $\times 10^3$
Case # 1	Aluminum plate	3.175	0.1524	71	0.33	2.7
Case # 2	Stainless steel plate	1.588	0.1524	205	0.3	7.8
Case # 3	Composite plate (isotropic)	5.588	0.1524	33	0.25	1.811

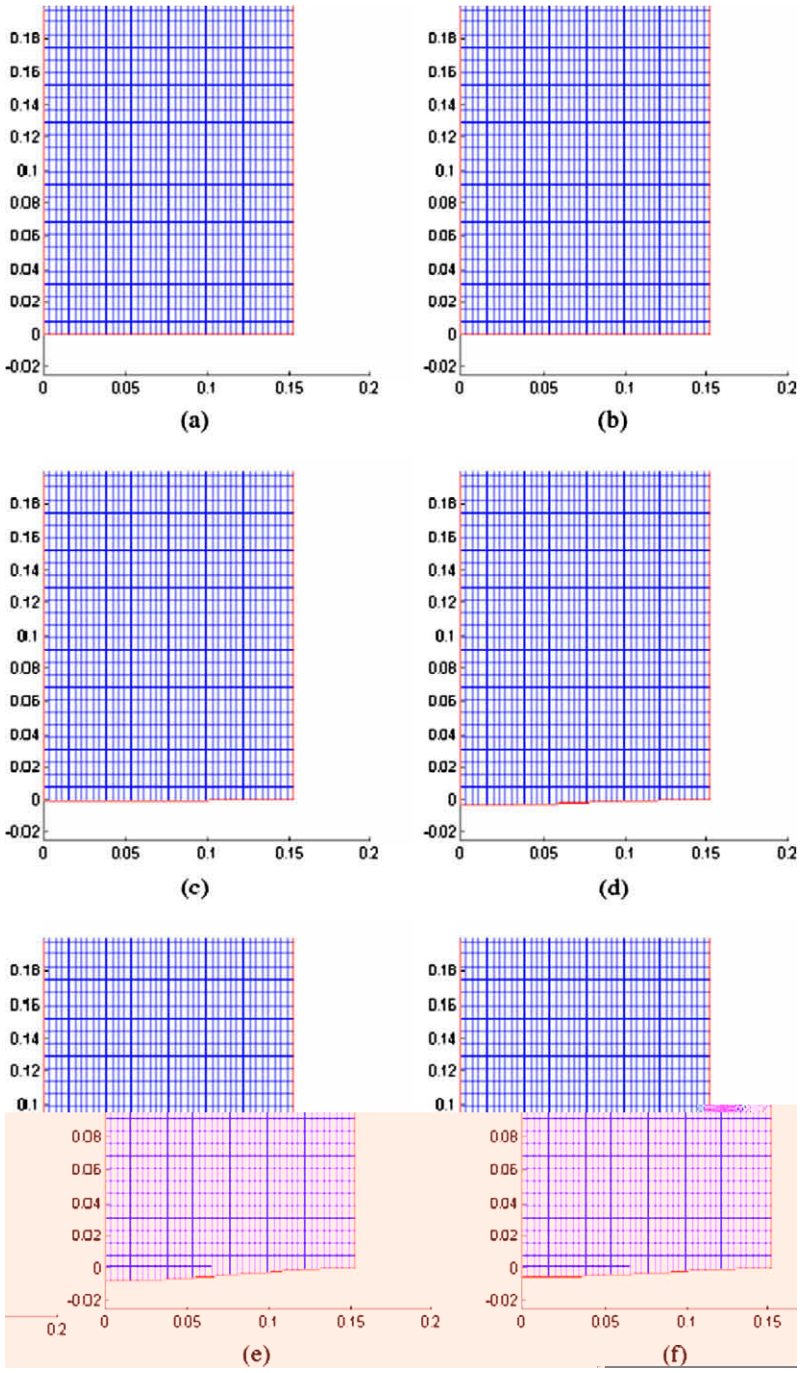

Fig. 10. Interaction of shock wave and clamped circular aluminum plate: mesh corresponds to the results shown in Fig. 11.

decreases, as shown in Fig. 13(b). Since the plate is modelled as linear elastic, such damping phenomena are solely attributed to the fluid–structure interaction. Due to the fact that the fluid structure interaction at the rear (non impact) side surface of the plate was not modelled in this simulation, it is expected that such damping effect will double if the interaction is fully modelled on both sides of the plate. Other factors such as viscosity and plastic dissipation may also contribute to the damping effect.

It should also be noticed that the plate reaches its maximum transverse displacement at the center, while the maximum stress occurs next to the edge where the plate is fully clamped. The maximum stress history was plotted in Fig. 13(c).

Strain on the plate surface can be obtained from the numerical results at the element's Gauss integration point. The stress on the surface of the plate can be calculated by:

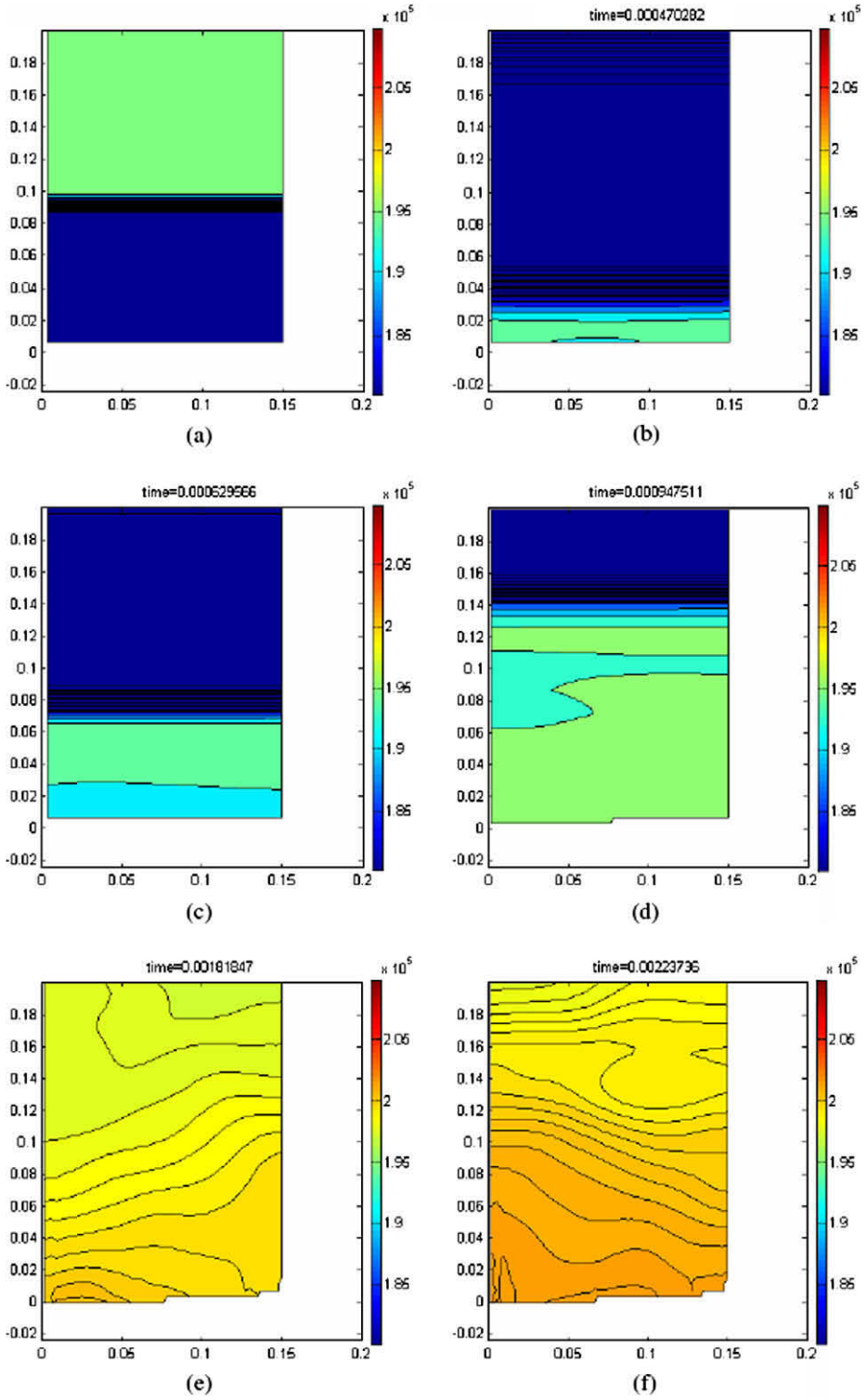

Fig. 11. Interaction of shock wave and clamped circular aluminum plate: pressure contours 1.

$$\sigma_r = -\frac{6M_r}{h^2} \tag{42}$$

where σ_r is the stress along the radial direction, M_r is the bending momentum acting along the radial direction, which was obtained in the numerical simulation. In the case of a thin circular plate, M_r can be expressed as:

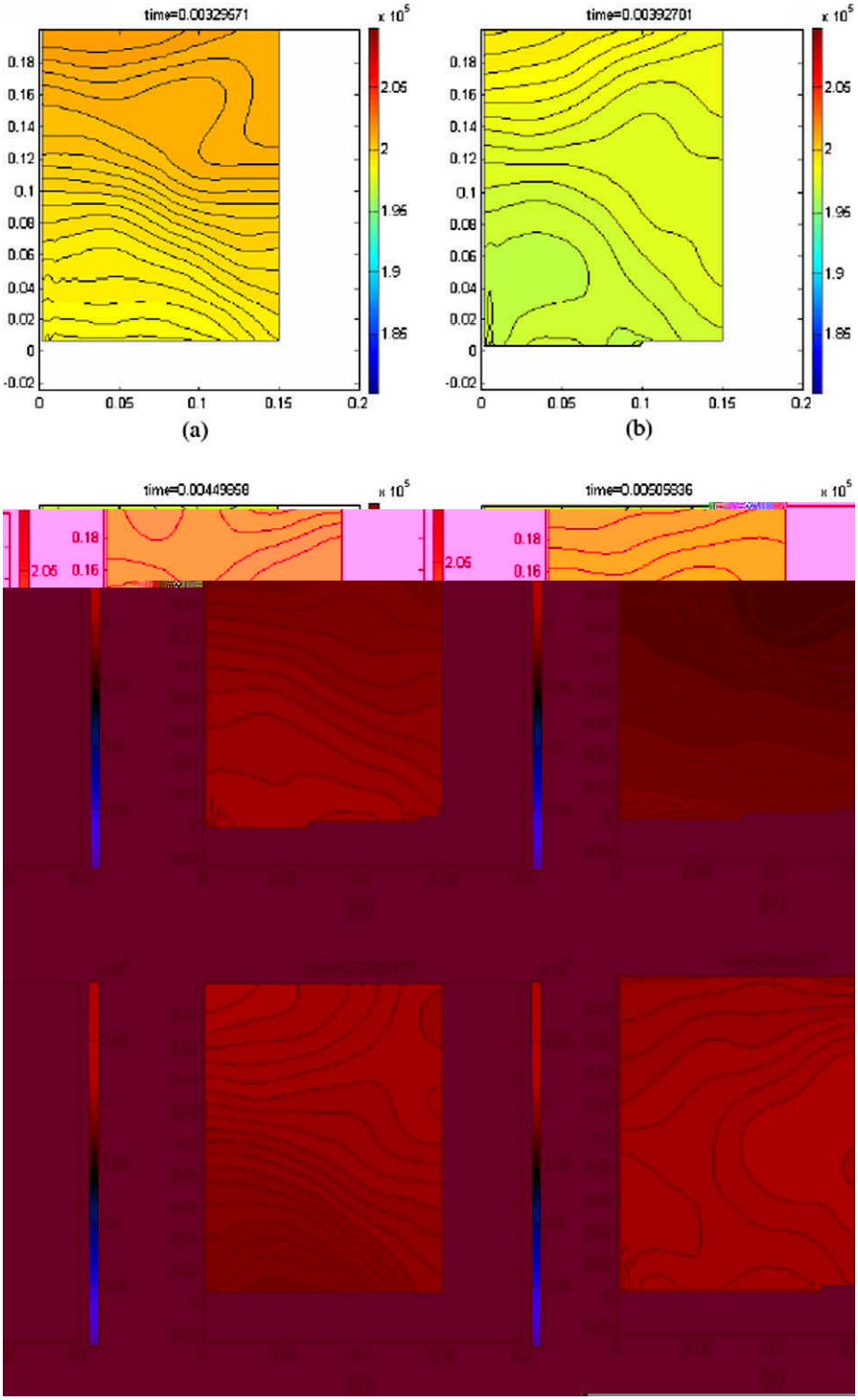

Fig. 12. Interaction of shock wave and clamped circular aluminum plate: pressure contours 2.

$$M_r = -D\left(\frac{\mathrm{d}^2 w}{\mathrm{d}r^2} + \frac{v}{r}\frac{\mathrm{d}w}{\mathrm{d}r}\right) \tag{43}$$

Details of the above relationship can be found in [27]. Once the surface stress σ_r is known, we can further calculate the surface strain along radial direction as:

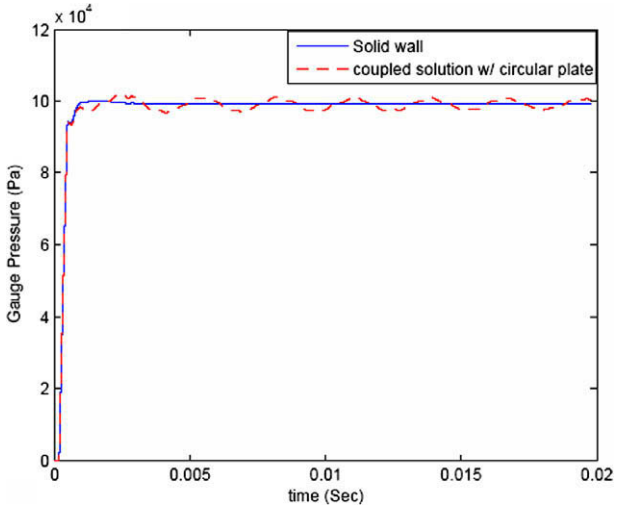

Fig. 13(a). Interaction of shock wave and clamped circular aluminum plate: center pressure loading.

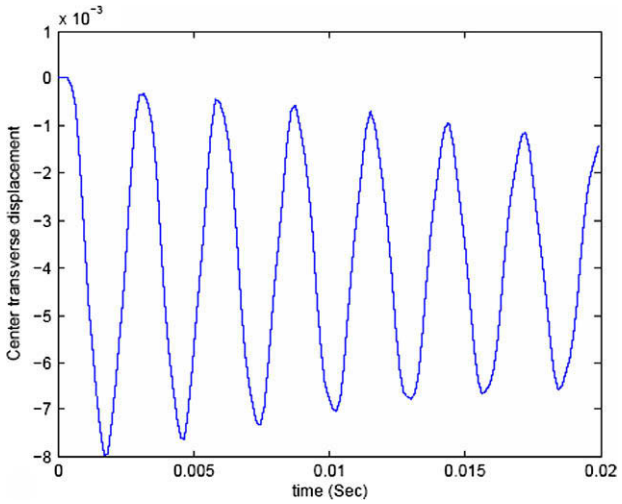

Fig. 13(b). Interaction of shock wave and clamped circular aluminum plate: center transverse displacement.

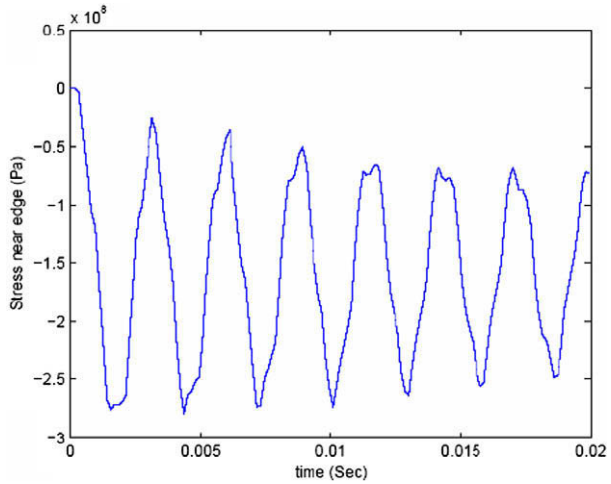

Fig. 13(c). Interaction of shock wave and clamped circular aluminum plate: stress history near clamped edge.

$$\varepsilon_r = \frac{(1-\nu^2)\sigma_r}{E} \tag{44}$$

where ν is the plate's Poisson's ratio and E is the modulus of elasticity.

Surface strain history at $r = 0.127$ m is plotted in Fig. 13(e) and its corresponding transverse displacement is plotted in Fig. 13(d). Strain signal history shows that several different modes have contributed to the fluctuation of strain. The power spectral density of the strain signal is calculated and plotted in Fig. 13(f). Notice that as the time step used in the numerical simulations is not a constant, before performing the Fast Fourier Transformation, sampling was performed by linearly interpolating the strain signal on constant time intervals. The 145 time steps originally obtained from simulation result was extended to a total of 256 uniform intervals. As the total time duration is 20 ms, the frequency window of FFT is 50 Hz. From the power spectral density data, we can obtain three peaks at 350 Hz, 1400 Hz, 3100 Hz, which are quite close to the experimentally obtained results listed in Table 2.

Further attempts were made to compare this numerical surface strain history along the radial direction with the experimental results of G&A obtained with a slightly higher pressure. The experimental results show that the strain signal fluctuates at a principle frequency of the second mode, while the numerical results fail to predict such frequency. This can be attributed to the fact that the current plate is modelled as perfect linear elastic, while the actual plate is exhibiting significant plasticity. It was observed that permanent deformation occured during the experiment, as shown in the experimental strain history. While the plate is plastic and experiencing permanent deformation, most of the kinetic energy transferred from the shock wave to the plate was absolved by the plastic deformation. As a result, the plate was vibrating at a dominant frequency of higher modes. To isolate the effect of first mode vibration, the surface strain signal was filtered with a fourth order

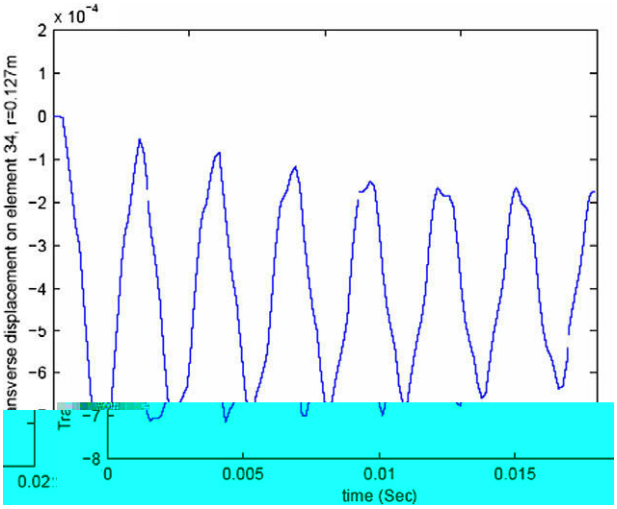

Fig. 13(d). Interaction of shock wave and clamped circular aluminum plate: transverse displacement at $r = 0.127$.

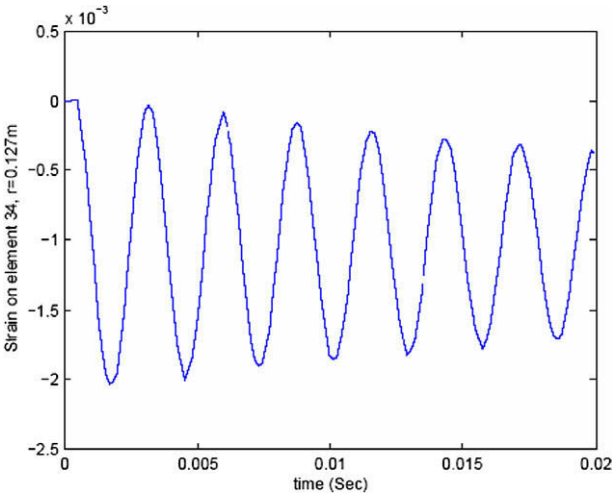

Fig. 13(e). Interaction of shock wave and clamped circular aluminum plate: surface strain at $r = 0.127$.

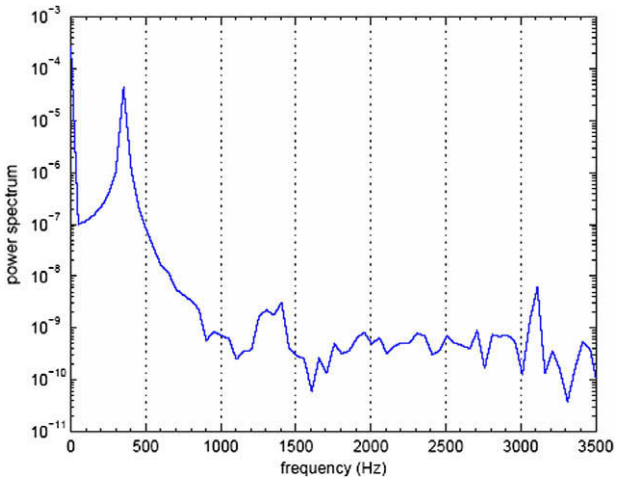

Fig. 13(f). Interaction of shock wave and clamped circular aluminum plate: power spectral densities of strain at $r = 0.127$.

Table 2
Modal analysis results of experimental data.

n	Mode m				
	1 (Hz)	2 (Hz)	3 (Hz)	4 (Hz)	5 (Hz)
Aluminum plate					
1	335	1373	3080	5436	
2	732	2075	4058		
3	1190	2838	5157		
Stainless steal plate					
1	184	701	1499	2655	4150
2	335	1068	2197	3326	5001
3	549	1373	2410	4150	5257
Quasi-isotropic composite plate					
1	396	1953	4700	7200	–
2	1220	2600	5859	–	–
3	1700	4500	–	–	–

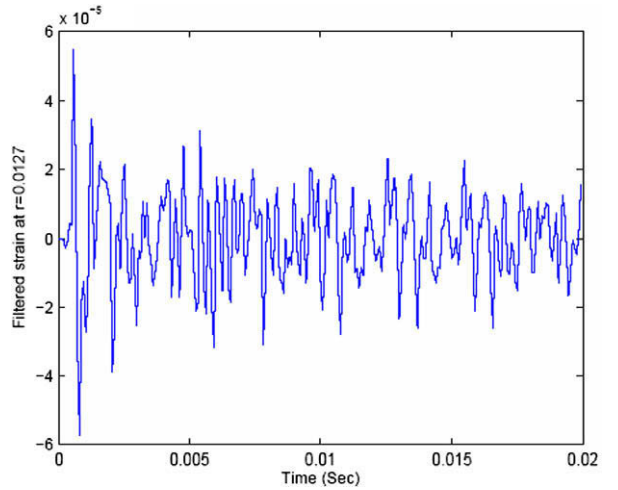

Fig. 13(g). Interaction of shock wave and clamped circular aluminum plate: filtered surface strain at $r = 0.127$.

Butterworth high pass filter at a cutoff frequency of 1000 Hz. The filtered strain signal is shown in Fig. 13(g), with most of the first mode frequency component being eliminated. As expected, comparing this filtered signal with the experimental data, the fluctuation of the strain is about 80×10^{-6} peak to peak, which is about the same magnitude as obtained from the experimental result.

10.2. Grid dependency and validation

Gird dependency tests were conducted to ensure that the physical phenomena simulated numerically through out this research do not rely on the resolution of the numerical grid. An initial mesh of 21×21 was chosen to perform the same

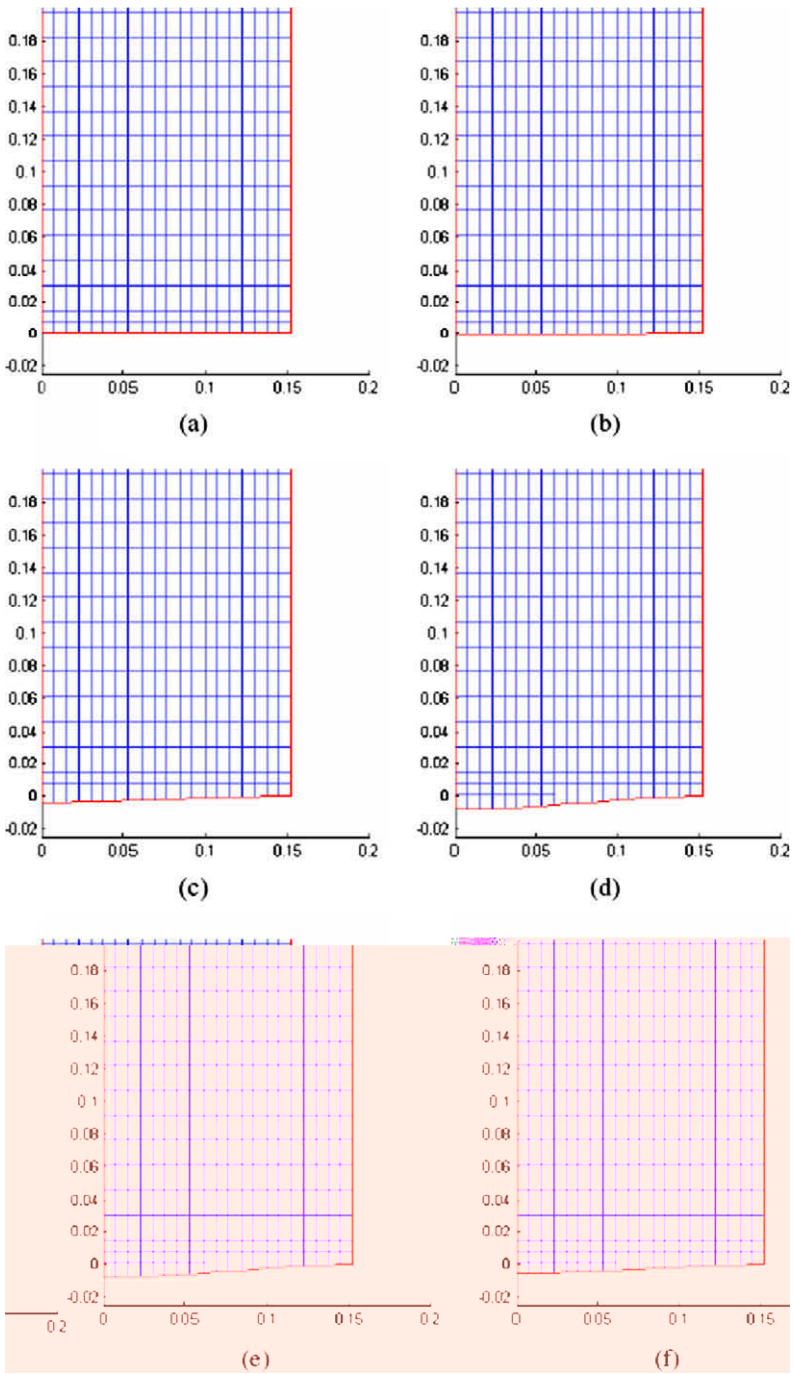

Fig. 14. Interaction of shock wave and clamped circular aluminum plate: mesh corresponding to Fig. 15. Initial mesh set as 21×21.

numerical simulation in the case of shock wave interaction with a clamped circular aluminum plate. All initial conditions, boundary conditions and physical properties were set to be the same as those used in numerical simulation with a 41×41 initial mesh. The meshes at different time levels are plotted in Fig. 14. The corresponding pressure contours are shown in Fig. 10. Because the different time steps used in numerical simulations performed with different meshes, the time levels in these plots are not exactly the same as those shown in Figs. 10–12. However, closest time levels are chosen for

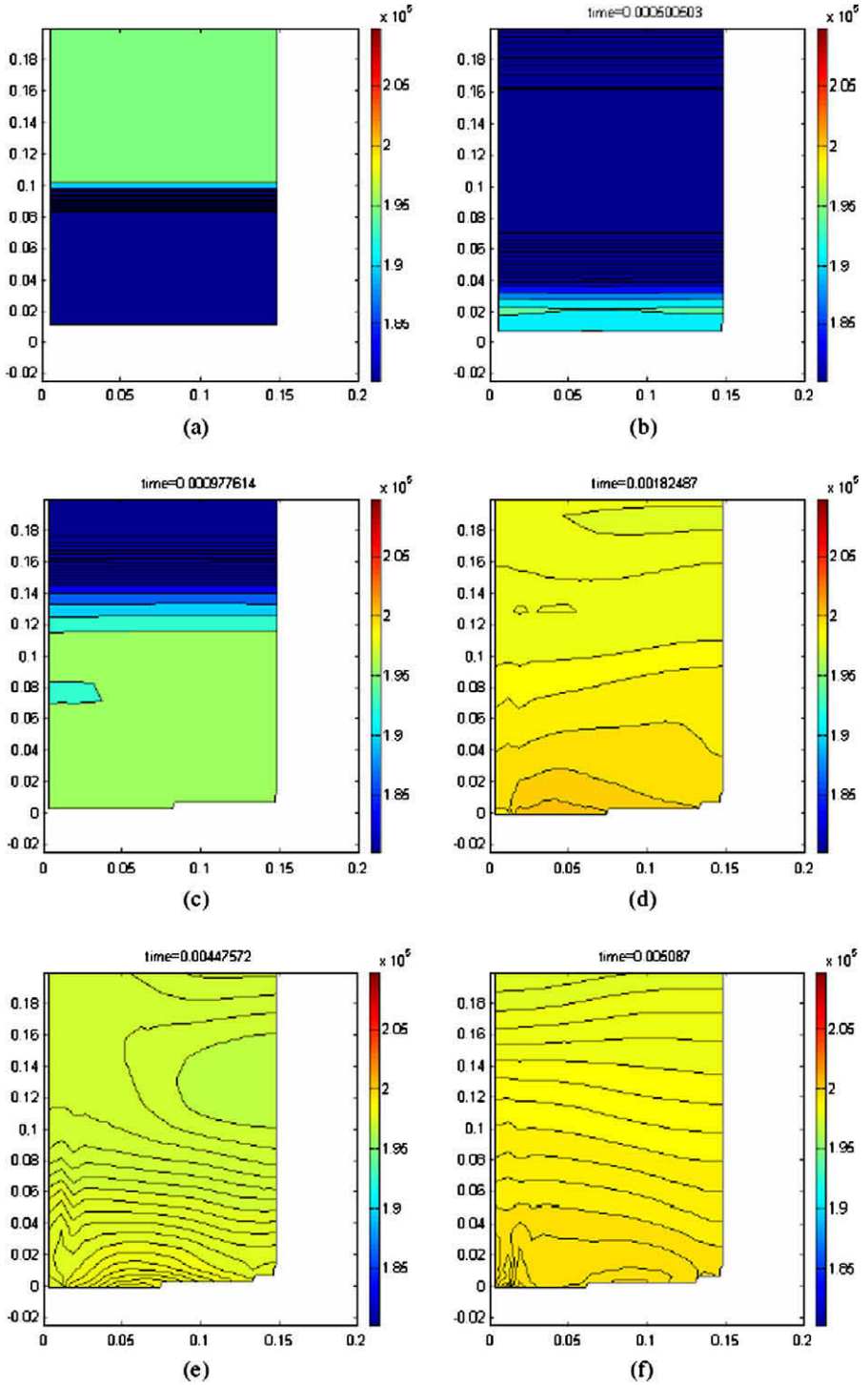

Fig. 15. Interaction of shock wave and clamped circular aluminum plate: pressure contours 1. Initial mesh set as 21×21.

comparison. Fig. 15(a)–(f) show pressure contours at different times obtained with the lower resolution grid. These figures can be directly compared with pressure contours shown in Figs. 11(a), (b), (d) and (e) and 12(c) and (d). It can be seen that the pressure contours with finer meshes may have a slightly higher spatial resolution, other than that the pressure contours are in very similar pattern and of the same magnitude at approximate the same time levels.

Such grid independency can be further observed in Fig. 16(a) where the pressure signals are plotted. In Fig. 16(b) the center transverse displacements are plotted and compared.

10.3. Interaction of shock wave and clamped circular stainless steel plate

In this simulation the same mesh, initial and boundary conditions are used as those used in the previous Section 6.1. The only difference is that here a stainless steel plate is used with the corresponding material properties shown in Table 1.

The shock wave reflection and acoustic wave generation patterns calculated in this interaction are similar to the case of aluminum plate, except that different time scales are involved because the stainless steel plate used in this simulation has lower natural frequencies due to its lower flexural rigidity.

The pressure history at the plate center is plotted in Fig. 17(a) along with the case with shock wave reflection off a rigid wall. Pressure fluctuation is also observed in this case. Compare with the case of aluminum plate, the magnitude of this

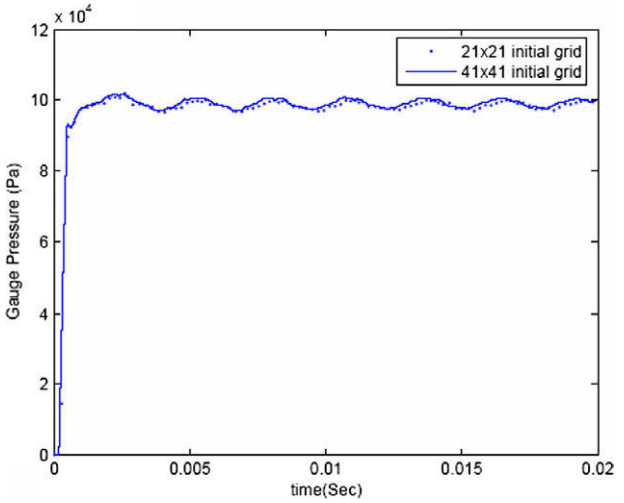

Fig. 16(a). Interaction of shock wave and clamped circular aluminum plate: comparison of center pressure loadings obtained with two different size meshes.

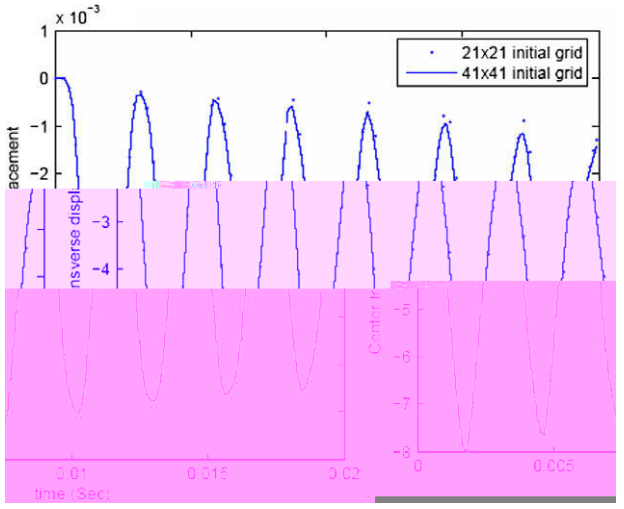

Fig. 16(b). Interaction of shock wave and clamped circular aluminum plate: comparison of center transverse displacement obtained with two different size meshes.

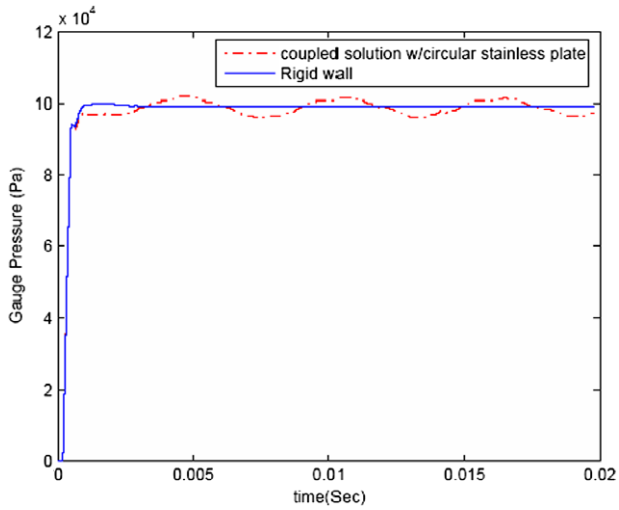

Fig. 17(a). Interaction of shock wave and clamped circular stainless steel plate: center pressure loading.

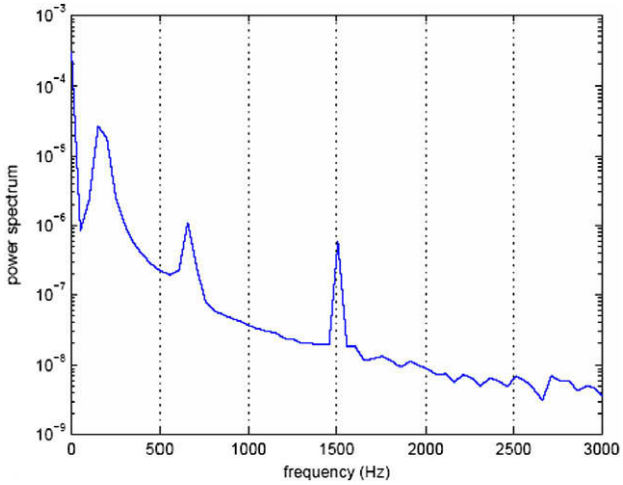

Fig. 17(b). Interaction of shock wave and clamped circular stainless steel plate: power spectral densities of strain at $r = 0.063$.

pressure fluctuation is larger, with a lower characteristic frequency. This frequency is about 170 Hz, which is the first natural frequency calculated theoretically (see G&A) and it is very close to the measured value of 184 Hz listed in Table 2.

The power spectral density of the strain at $r = 0.063$ m shown in Fig. 17(b) clearly demonstrates 3 major peaks at 170 Hz, 650 Hz and 1500 Hz. These frequencies agree well with those calculated by other methods (see G&A) as well with experimental data shown in Table 2.

However, the strain history of the plate at $r = 0.089$ m has totally different behavior than that obtained at location $r = 0.063$ m. Power spectral density of this simulated strain (see Fig. 17(c)) shows 3 major peaks at 650 Hz, 1500 Hz and 2700 Hz, which corresponding to the second, third and fourth natural frequencies of the plate. This location is very close to $r = 0.618\alpha$ (where α is the radius), which is the nodal point of the first mode vibration at 170 Hz. So the strain history is almost not affected by the first mode vibration of the plate, neither significantly altered because of the permanent deformation of the stainless plate.

10.4. Interaction of shock wave and clamped circular quasi-isotropic composite plate

In this simulation the same mesh, initial and boundary conditions are used as those used in the case of metallic plate. The material properties used for the quasi-isotropic composite plate are shown in Table 1.

The phenomena related to shock wave reflection and acoustic wave generation patterns are similar to the case of metallic plates, except that different time scales are involved because the composite plate used in this simulation has higher natural frequencies.

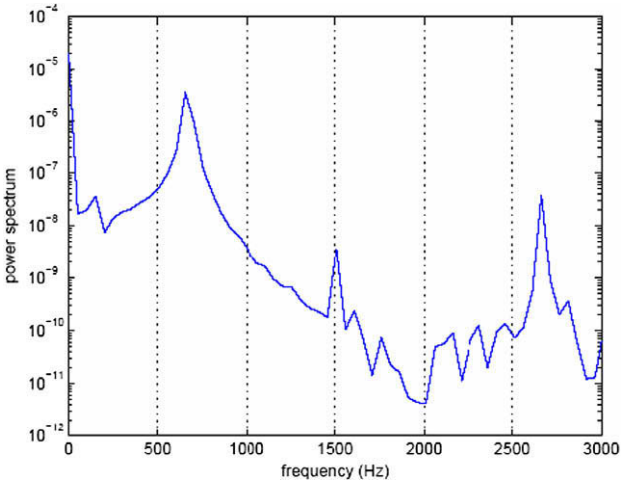

Fig. 17(c). Interaction of shock wave and clamped circular stainless steel plate: power spectral densities of strain at $r = 0.089$.

The pressure history at the plate center is plotted in Fig. 18(a) along with the case with shock wave reflection off a rigid wall. Pressure fluctuation is also observed in this case. The magnitude of this pressure fluctuation is small because this plate has a larger flexural rigidity and the center transverse displacement is small compared with that of the metallic plates. The pressure fluctuation frequency is about 480 Hz, which according to G&A is the first natural frequency calculated theoretically.

The power spectrum of the strain is plotted in Fig. 18(b). Three major peaks are observed at about 480 Hz, 1900 Hz and 4300 Hz. The second and third modal frequencies are in excellent agreement with the experimental data listed in Table 2. The dominant frequency observed in the experiment is at about 400 Hz, which is by about 16% lower than that computed in the present simulations. This suggests that the actual composite plate may have a lower flexural rigidity than what used in the computations, which was calculated using a simple formula for isotropic material. Further calculations show that a reduced flexural rigidity at 80% of the original values used will yield better agreement between experiment and numerical simulations.

10.5. Non-linear behavior in the interaction

The experimental work of G&A has indicated that during the interaction of shock waves with the plates, their vibration was dominated by several modes. Comparison of the magnitude of these modes obtained from experiments with those from theoretical analyses or numerical simulations has shown that modal suppression can take place possibly as a result of the non-linear plastic deformation of the plate. Experimental results also show that there exists several extra peaks in the resonance signal power spectrum besides those from the basic modal frequencies of the plate. It has been suggested in G&A that these peaks may belong to the subharmonic and high harmonic of the acoustic excitation as a result of both non-linear vibration of the plate and non-linear propagation of the pressure waves. With the aid of the numerical results obtained in the present work, we can further investigate this non-linear coupling process between the structure and shock wave during their interaction. Hence we introduce the *phase diagram* and *Poincare map* to further investigate this non-linear behavior.

Phase diagram and Poincare map are effective tools in the study of non-linear system. The relevant theories and their application can be found in [28]. Phase diagram can be obtained by plotting the time derivative of a quantity against the quantity, and a typical Poincare map can be obtained by plotting the $(n+1)$th local maximum of the time series against the nth local maximum. For an ideal sinusoidal time series, the phase diagram is circular and the Poincare maps will reduce to a point. The phase diagram of a non-linear time series will have heavier circular lines due to the lack of precise periodicity or the lines will not be circular at all if the time series is highly non-linear. Similarly, the Poincare map for a non-linear system will have several spaced regions. In the case of a chaotic system, Poincare map points will be spreading all over the region. In the following, phase diagrams and Poincare maps are obtained by further processing the time series data. In plotting Poincare maps, local extrema of the time series are needed and usually this process is not a trivial task. A Matlab code was written which took advantage of the Matlab index operation and thus all local extrema could be found effectively using a few line of codes. However, if identification of shock waves or blast waves peak is needed, a more advanced algorithm is needed and the typical work is illustrated in [29].

10.6. Non-linear vibration of the plate

The phase diagrams and Poincare maps of the plate center displacement under shock wave impact are plotted in Figs. 19–21. The center displacement phase diagram of all three plates is not circular, however, still follows a loop pattern. This

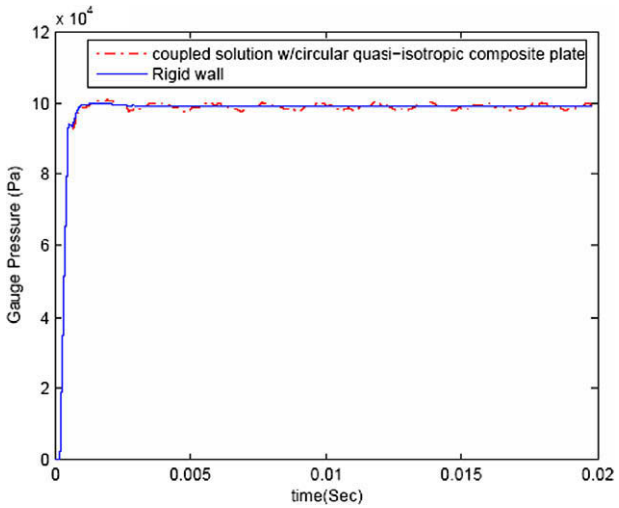

Fig. 18(a). Interaction of shock wave and clamped circular quasi-isotropic composite plate: center pressure loading.

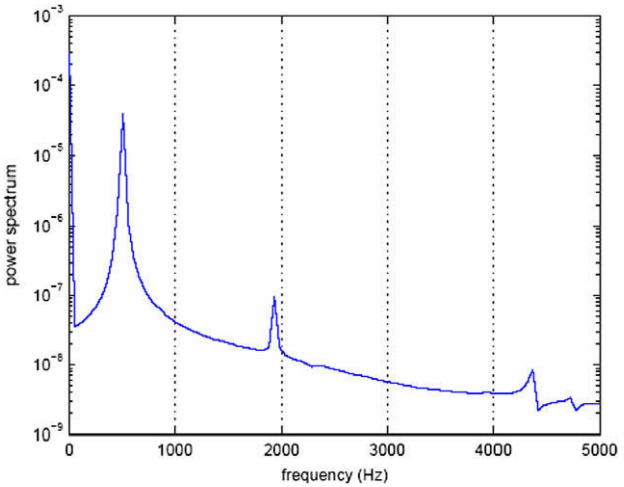

Fig. 18(b). Interaction of shock wave and clamped circular quasi-isotropic composite plate: power spectral densities of strain at $r = 0.140$.

suggests that there is non-linearity involved in the vibration of the plate, but this non-linearity is not dominant such that the vibrations still exhibit certain periodicity. The Poincare maps also showing slightly spreading of the extrema points, but these points are still clustered, thus such non-linearity is not dominant. Comparing the Poincare maps of the different plates, it appears that the stainless steel plate has the most spreading on the map, while the composite plate has the least. This suggests that this non-linearity is related to the displacement magnitude of the plate, where the stainless steel plate has the largest displacement and the composite plate has the smallest. Because all plates are modelled as linear in the finite element code, the source of this behavior should be solely attributed to the interaction process, where the loading on the plate is not uniform or perfectly periodic.

The non-linear pressure loading on the plate can be further analyzed using an approach similar to that described above. The phase diagrams and Poincare maps of plates center pressure loading during the interaction are plotted in Figs. 22–24. From the time history plot, we can already see that all these pressure histories are not perfectly sinusoid, even though there exists certain periodicity. It appears that the pressure history with the stainless steel is the cleanest while that with the composite is of the opposite. The phase diagram of the pressure in the case of stainless steel plate is less chaotic and certain loops can still be observed, while in the case of the composite plate, lines have been crossing each other heavily thus it appears that the pressure loading on the composite is highly non-linear. All Poincare maps are showing considerable spreading. However, in the case of stainless steel plate, most of the points are linearly correlated along the diagonal line. In the case of the composite plate, such spreading has a different pattern, where those points seem to be clustered around two loops. Such kind of clustering suggests the existence of non-linear harmonics or subharmonics in the pressure time history.

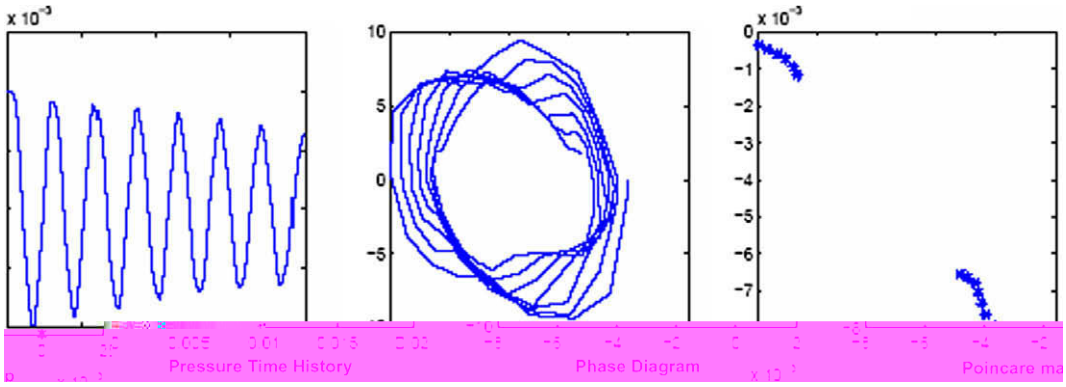

Fig. 19. Center displacement, phase diagram and Poincare map in the case of aluminum plate.

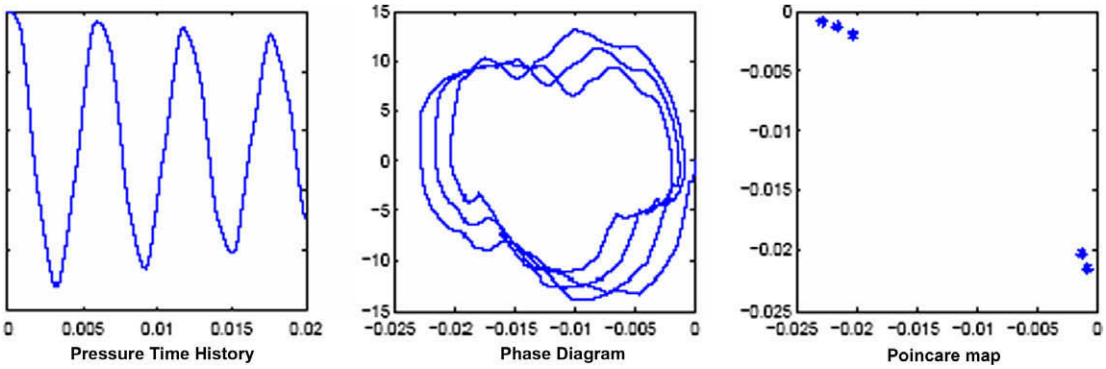

Fig. 20. Center displacement, phase diagram and Poincare map in the case of stainless steel plate.

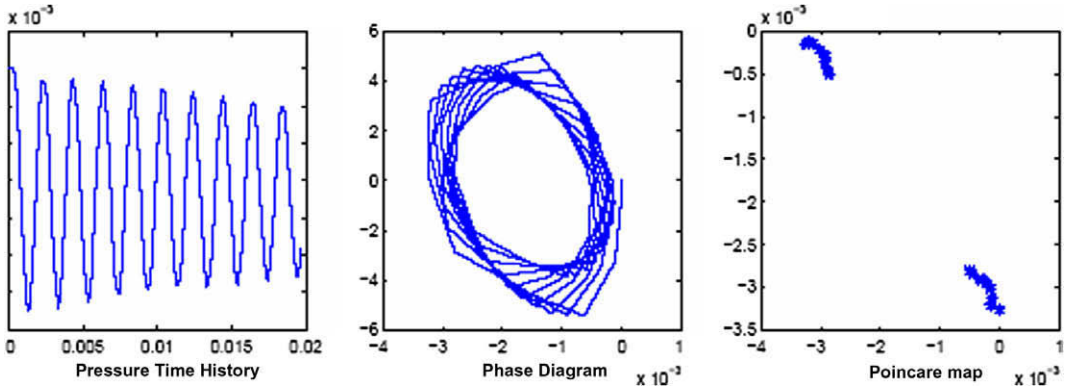

Fig. 21. Center displacement, phase diagram and Poincare map in the case of composite plate.

These non-linear frequency characteristics are further illustrated in Fig. 25, where the power spectral densities of the plates' center pressure are plotted. In these plots, besides the major peaks which belong to the natural frequency of the plate vibration modes, there also exist many other peaks of smaller amplitude. More interesting results can be obtained if we further compare the magnitude of the basic natural frequency peaks of each plate. In the case of stainless steel plate, the ratio between the first peak and second peak is at about 100, while for the aluminum plate it is about 50 and for the composite plate, it is only 10. This suggests that while the composite plate has a higher fundamental frequency and less center displacement, somehow its second modes have been amplified in the non-linear process. Yet in the analysis from the previous section, the center displacement of the composite plate is showing the least non-linearity. This behavior is further confirmed by

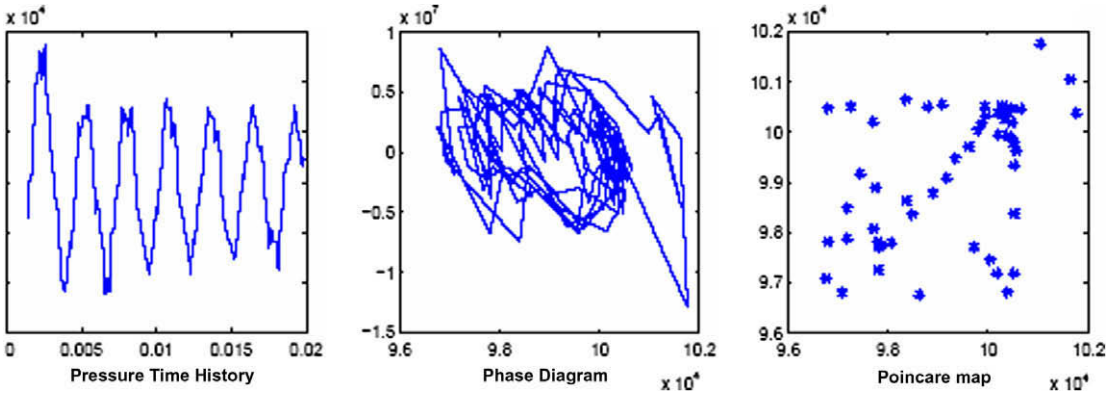

Fig. 22. Center pressure, phase diagram and Poincare map in the case of aluminum plate.

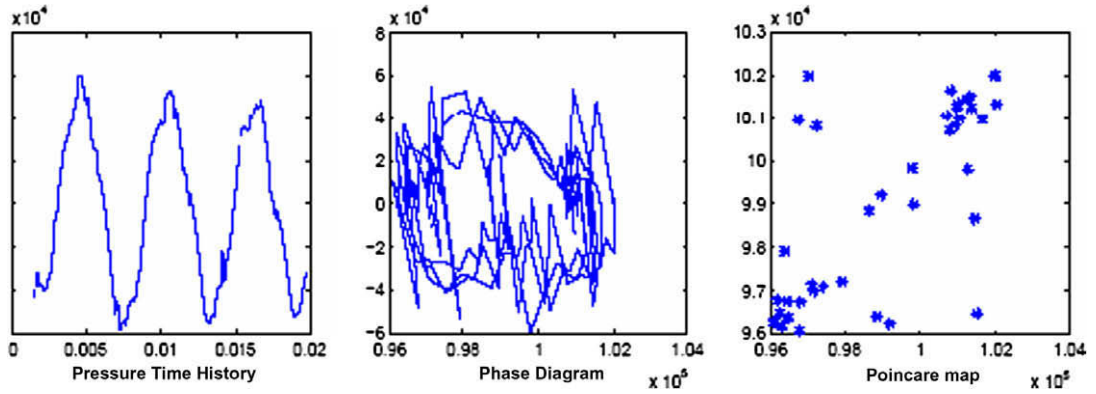

Fig. 23. Center pressure, phase diagram and Poincare map in the case of stainless steel plate.

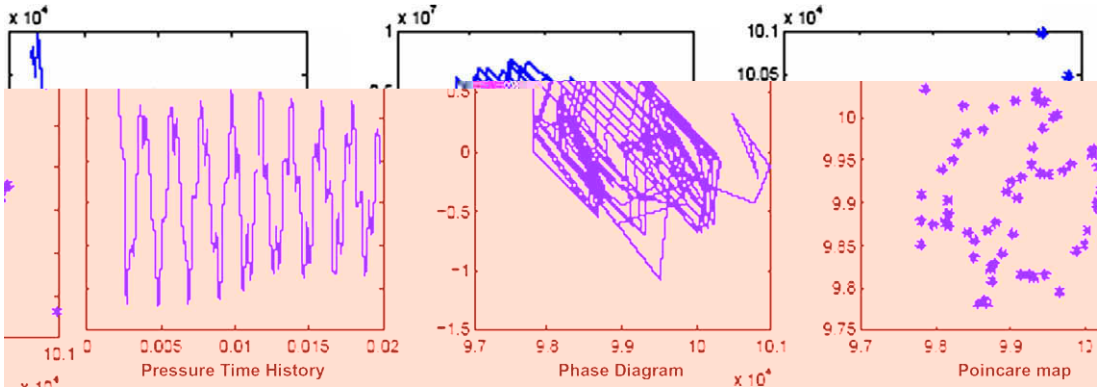

Fig. 24. Center pressure, phase diagram and Poincare map in the case of composite plate.

the experiment results of G&A, where the strain signal appears to be cleaner than that of the metallic plate, the acoustic resonance pressure is showing lots of small spikes in its spectra. Similar phenomena were also observed in the numerical simulations of Frendi et al. [12], where a plate excited by time harmonic, normally incident acoustic source, was found to generate acoustic waves propagating non-linearly into the far-field. The non-linear propagation of these pressure waves is a result of complicated interactions between these pressure waves themselves. To further investigate this phenomena, the one-dimensional non-linear propagation of pressure waves is considered.

The non-linear process starts as soon as the impact of the shock wave set the plate in motion. Such plate motion will again transfer energy into the flow fields and set the fluid in motion, which will result as a series of infinitesimal pressure waves, as illustrated typically in Fig. 1.

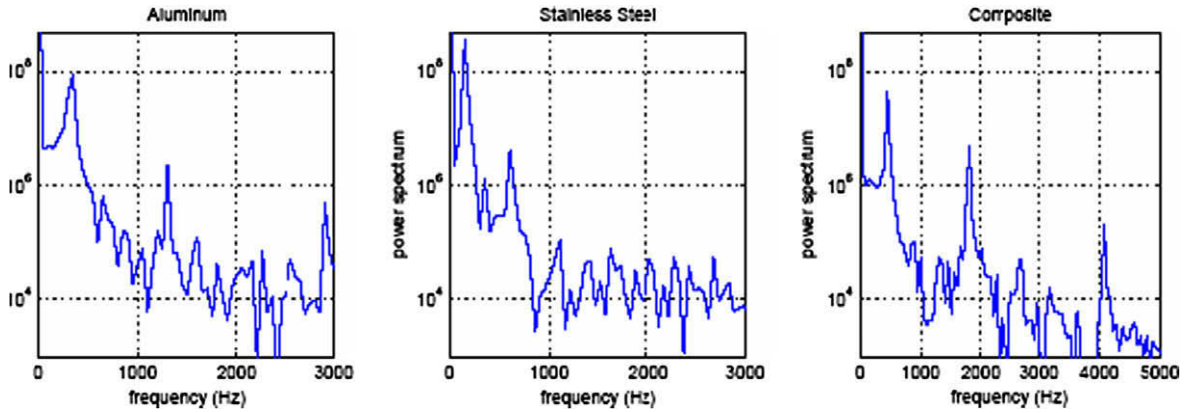

Fig. 25. Power spectral densities of pressure at plates' center.

If the plate is vibrating periodically with a series of modes, we can assume a simple form of its transverse displacement velocity as:

$$u(t) = \sum A_i \sin \omega_i t \tag{45}$$

where A_i is the magnitude of the plate transverse displacement velocity belongs to the ith mode and ω_i is the ith modal frequency of the plate.

The plate ith mode transverse displacement is:

$$x_i = \int_0^t u_i(t)\mathrm{d}t = \frac{A_i}{\omega_i}(1 - \cos \omega_i t) \tag{46}$$

As the acoustic wave travels through the fluid, it imparts velocity to its particles and creates infinitesimal changes in the fluid properties. The flow properties across these waves can be modelled by considering the propagation of a wave of finite amplitude into an inviscid compressible fluid in a constant cross-sectional area duct, and assuming the duct flow to be frictionless with no heat interaction, i.e. the flow is adiabatic, and that the fluid ahead of the wave has uniform properties, p, ρ, T. The analysis used here is similar to that in [30]

$$\begin{aligned} x &= (u + a)t + f(u) \\ u &- \frac{2a}{\gamma - 1} = K \end{aligned} \tag{47}$$

Here K is referred to as Riemann Invariable along the characteristic line, $(u + a)$ is the right-running wave propagation speed, its relationship with pressure is:

$$\frac{\mathrm{d}}{\mathrm{d}p}(u + a) = \frac{\mathrm{d}u}{\mathrm{d}p} + \frac{\mathrm{d}a}{\mathrm{d}p} \tag{48}$$

With the help of perturbation method and the perfect gas relationship, this characteristic relationship can be further expressed as:

$$\frac{\mathrm{d}}{\mathrm{d}p}(u + a) = \frac{1}{2\rho^4 a^3}\left(\frac{\mathrm{d}^2 p}{\mathrm{d}v^2}\right)_s \tag{49}$$

where $v = \frac{1}{\rho}$ is the specific volume.

This equation shows the relationship between wave propagation and pressure. Form the temperature–pressure relationship for perfect gas, $pv^\gamma = C$,

$$\frac{\mathrm{d}^2 p}{\mathrm{d}v^2} = \frac{\gamma(\gamma + 1)p}{v^2} > 0 \tag{50}$$

Subsequently we have

$$\frac{\mathrm{d}}{\mathrm{d}p}(u + a) > 0 \tag{51}$$

Thus if the wave is travelling in the same direction as the particle, increasing of pressure will result in an increase of the waves travelling velocity $u + a$. This means that the compression waves formed by the right hand-side acceleration of the plate will steepen as they travel along the duct, and the compression region tending to coalesce into a shock wave. For

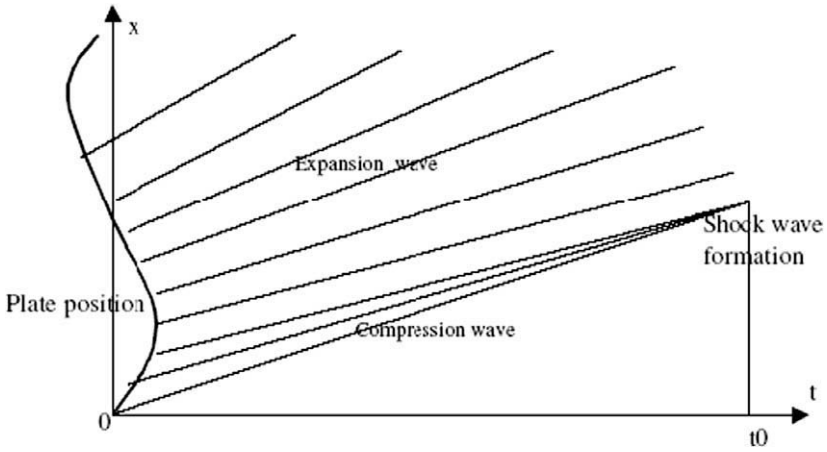

Fig. 26. Steepening of compression waves and the formation of a shock wave.

the expansion waves formed by the left hand-side acceleration of the plate, it tends to spread wider as a result of the reduction in pressure. This will result in a distortion of the original waves emitted from the fluid–structure interface. A sinusoidal wave will no longer be sinusoidal while experiencing non-linear phase and frequency shift. Under extreme condition the compression of the wavefront may eventually reaches a point where a shock forms. This compression waves steepening and shock wave formation process is illustrated in Fig. 26.

In this figure t_0 is the time when the steepening of the compression wave is maximum and a shock is formed. Notice that at this point isentropic flow ceases to be valid because of the large gradients in the flow variables. If, however, the shock is pursued further with the assumption of isentropic flow, then at the location where the shock is formed, $\left(\frac{\partial u}{\partial x}\right)_t$ tends to be infinity. Equivalently, we have:

$$\left(\frac{\partial x}{\partial u}\right)_t|_{u=0} = 0 \tag{52}$$

This gives the shock wave forming condition. From the aforementioned wave relation in Eq. (47), we have:

$$\begin{aligned} a &= a_1 + \frac{\gamma-1}{2}u \\ x &= \left(a_1 + \frac{\gamma+1}{2}u\right)t + f(u) \end{aligned} \tag{53}$$

where a_1 is the sound speed of the quiescent area before the compression wave arrives. Take the derivative of x with regard to u at $u = 0$ and make the derivative to be zero, we have the shock wave formation time:

$$t_s = -\frac{2}{\gamma+1}f'(0) \tag{54}$$

Yet the expression of $f(u)$ is to be determined from the boundary condition. At the exact interface between the plate and structure, we have

$$x_p = \frac{A_i}{\omega_i}(1-\cos\omega_i t) = \left(a_1 + \frac{\gamma+1}{2}u_p\right)t + f(u) \tag{55}$$

where subscript p indicate properties at the plate and structure interface. We can express all t in terms of u. With $t = \arcsin\frac{u_p}{A_i}$ and $\cos\omega_i t = \sqrt{1-\frac{u_p^2}{A_i^2}}$, we have:

$$\frac{A_i}{\omega_i}\left(1-\sqrt{1-\frac{u_p^2}{A_i^2}}\right) = \frac{1}{\omega_i}\left(a_1 + \frac{\gamma+1}{2}u_p\right)\arcsin\frac{u_p}{A_i} + f(u) \tag{56}$$

From this we can get the expressions for $f(u)$ and $f'(u)$ as:

$$f(u) = \frac{A_i}{\omega_i}\left(1-\sqrt{1-\frac{u^2}{A_i^2}}\right) - \frac{1}{\omega_i}\left(a_1 + \frac{\gamma+1}{2}u\right)\arcsin\frac{u}{A_i} \tag{57}$$

$$f'(u) = \frac{A_i}{\omega_i}\frac{\frac{u}{A_i^2}}{\sqrt{1-\frac{u^2}{A_i^2}}} - \frac{\gamma+1}{2\omega_i}\arcsin\frac{u}{A_i} - \frac{1}{\omega_i A_i}\left(a_1 + \frac{\gamma+1}{2}u\right)\frac{1}{\sqrt{1-\frac{u^2}{A_i^2}}} \tag{58}$$

So the shock wave is forming at time t_s:

$$t_s = -\frac{2}{\gamma+1} f'(0) = \frac{2}{\gamma+1}\left(\frac{a_1}{\omega_i A_i} + \frac{\gamma+1}{2}\frac{k\pi}{\omega_i}\right) \tag{59}$$

where $k = 0, 1, \ldots, N$. For $k = 0$, the shock wave forms at time:

$$t_s = \frac{2}{\gamma+1}\frac{a_1}{\omega_i A_i}$$

And the location of shock wave formation x_s is:

$$x_s = a_1 t_s + f(0) = \frac{2}{\gamma+1}\frac{a_1^2}{\omega_i A_i} + f(0)$$

Typical shock wave formation time for a plate vibrating at a frequency of 1 kHz and maximum transverse displacement of 0.01 m is about 0.72 ms. The corresponding shock wave is formed at 0.24 m away from the plate. Though shock wave is not presented on the plate during the interaction if all waves are assumed to be propagating one-dimensionally apart from the plate with the above derivation, the compression of the wavefront starts immediately at the fluid–structure interface, that results in a non-linear behavior of the pressure fluctuation. Furthermore as the plate is not vibrating like a piston, the pressure waves will not propagating one-dimensionally, but rather in a two-dimensional manner while complicated interactions and reflections occur. Such complicated pressure wave patterns can also be observed in the pressure contours from numerical simulations. These non-linear propagation of pressure waves can further complicate the loading on the plate, result in the non-linear vibration of the plate itself, further cascading the non-linearity. From the above analysis we can also see that the faster the plate is vibrating, and the higher the vibrating frequency is, the stronger such non-linear effects will be. Because of this, the composite plate exhibits the highest non-linear effects on the pressure fluctuation since its natural frequency is higher, and such non-linear behavior is more evident on the higher frequency modes.

Another characteristic scale associated with non-linearity arises during the interaction process, which is the relationship between the characteristic time scale of the plate represented by its natural frequency modes and the time scale of the pressure wave propagation represented by the sound speed inside the fluid flow field. It appears that the non-linearity is intensified when the plate is vibrating at high frequency while the wave propagation speed is low.

11. Conclusions and final remarks

A fully coupled aeroelastic solver was developed, tested and implemented to solve the problem of shock wave impingement on elastic solid-phase surfaces. The novelty in the present approach relies on a two way fluid–structure interaction problem. The method is based on an unstructured adaptive mesh high resolution flow solver with shock capturing capability, a finite element structure solver and a moving mesh algorithm. A new advancing front moving mesh fully conservative first order accurate algorithm was made possible with the implementation of a flexible and efficient *quad-edge* data structure. Adaptive mesh refinement was also implemented for improved efficiency and accuracy.

Numerical simulations were performed on the interaction of a shock wave impacting aluminum, steel and composite plates. Numerical results were further validated by theoretical analysis, experiment data and results from other numerical simulations. Grid independence tests were performed and the results showed that the physical phenomena and quantities were independent of the numerical grid chosen in the simulation.

Modal response of the plate subject to shock wave loading was observed in the strain signal and compared with experiments, where non-linear plastic deformation contributes severely to the suppression of the first modes in the metallic plate cases. Aerodynamic damping of the plate vibration was reproduced in the numerical simulation without manually adding any damping coefficient.

Further non-linear analysis on the numerical results shows that the mutual interaction process is non-linear. Analysis shows that non-linearity arises because the wave propagation in the fluid is non-linear and it will further cascade a non-linear and non-uniform loading on the plate. Non-linearity intensifies when the plate is vibrating at high frequency while the wave propagation speed is low, which is characterized by the characteristic time scale of the plate vibration and pressure wave propagation.

There maybe other factors that will further intensify the non-linear behavior. Damping played an important role during the interaction and it is also one source of non-linearity.

Acknowledgment

The authors would like to acknowledge the financial support provided by the U.S. Army Research Development and Engineering Center (ARDEC) at Picatinny Arsenal.

References

[1] B. Hopkinson, British Ordnance Board Minutes, Report No. 13565. British Ordnance Office, London, 1915.
[2] G. Taylor, The Pressure and Impulse of Submarine Explosion Waves on Plates, The Scientific Papers of G.I. Taylor, vol. III, Cambridge University Press, Cambridge, UK, 1963.
[3] M. Gong, Y. Andreopoulos, Shock wave impact on monolithic and composite material plates: the preferential aeroelastic response, Journal of Sound and Vibration 313 (2008) 171–194.
[4] M. Gong, Mutual Interactions between Shock Waves and Structures, Ph.D. Thesis, City University of New York, 2006.
[5] R. Houlston, J.E. Slate, N. Pegg, C.G. DesRochers, On Analysis of structural response of ship panels subjected to air blast loading, Computers and Structures 26 (1987) 1–15.
[6] A.D. Gupta, F.H. Gregory, R.L. Bitting, S. Bhattacharya, Dynamic analysis of an explosively loaded hinged rectangular plate, Computers and Structures 26 (1987) 339–344.
[7] F.B.A. Beshara, Modeling of blast loading on aboveground structures – I. General phenomenology and external blast, Computers and Structures 51 (1994) 585–596.
[8] H.S. Turkmen, Z. Mecitoglu, Nonlinear structural response of laminated composite plates subjected to blast loading, American Institute of Aeronautics and Astronautics Journal 37 (1999) 1639–1647.
[9] H.S. Turkmen, Z. Mecitoglu, Dynamic response of stiffened laminated composite plate subjected to blast load, Journal of Sound and Vibration 221 (1999) 371–389.
[10] A.C. Jacinto, R.D. Ambrosini, R.F. Danesi, Experimental and computational analysis of plates under air blast loading, International Journal of Impact Engineering 25 (2001) 927–947.
[11] S. Chung Kim Yuen, G.N. Nurick, Experimental and numerical studies on the response of quadrangular stiffened plates. Part I: subjected to uniform blast load, International Journal of Impact Engineering 31 (2005) 55–83.
[12] A. Frendi, L. Maestrello, A. Bayliss, Coupling between plate vibration and acoustic radiation, Journal of Sound and Vibration 177 (1994) 207–226.
[13] A. Frendi, L. Maestrello, L. Ting, An efficient model for coupling structural vibrations with acoustic radiation, Journal of Sound and Vibration 182 (1995) 741–757.
[14] Z. Xue, J.W. Hutchinson, Preliminary assessment of sandwich plates subject to blast loads, International Journal of Mechanical Sciences 45 (2003) 687–705.
[15] Z. Xue, J.W. Hutchinson, A comparative study of impulse-resistant metal sandwich plates, International Journal of Impact Engineering 30 (2004) 1283–1305.
[16] R. Kamakoti, W. Shyy, Fluid–structure interaction for aeroelastic applications, Progress in Aerospace Sciences 40 (2004) 535–558.
[17] D. DeZeeuw, K.G. Powell, An adaptively refined Cartesian mesh solver for the Euler equations, Journal of Computational Physics 104 (1993) 56–68.
[18] W.D. Henshaw, D.W. Schwendeman, An adaptive numerical scheme for high-speed reactive flow on overlapping grids, Journal of Computational Physics 191 (2003) 420–432.
[19] C.W. Hirt, A.A. Amsden, J.L. Cook, An arbitrary Lagrangian–Eulerian computing method for all flow speeds, Journal of Computational Physics 135 (1997) 203–216. http://dx.doi.org/10.1006/jcph.1997.5702. 260732.
[20] J. Glimm, M.J. Graham, J. Grove, X.L. Li, T.M. Smith, D. Tan, F. Tangerman, Q. Zhang, Front tracking in two and three dimensions, Computers and Mathematics with Applications 35 (1998) 1–11.
[21] C.S. Peskin, Numerical analysis of blood flow in the heart, Journal of Computational Physics 25 (1977) 220–232.
[22] E. Balaras, Modeling complex boundaries using an external force field on fixed Cartesian grids in large-eddy simulations, Computers and Fluids 33 (2004) 375–382.
[23] C. Farhat, M. Lesoinne, P. Le Tallec, Load and motion transfer algorithms for fluid/structure interaction problems with non-matching discrete interfaces: Momentum and energy conservation optimal discretization and application to aeroelasticity, Computer Methods in Applied Mechanics and Engineering 157 (1998) 95–114.
[24] O.C. Zienkiewicz, R. Taylor, The Finite Element Method, Butterworth-Heinemann, 2000.
[25] L. Guibas, J. Stolfi, Primitives for the manipulation of general subdivisions and computation of Voronoi diagrams, ACM Transactions on Graphics 4 (1985) 74–123.
[26] K.-J. Bathe, Finite Element Procedures, Prentice-Hall, Englewood Cliffs, NJ, 1996.
[27] S. Timoshenko, S. Woinowsky-Krieger, Theory of Plates and Shells, second ed., McGraw Hill, 1959.
[28] S. Wiggins, Introduction to Applied Nonlinear Dynamical Systems and Chaos, Springer-Verlag, 1990.
[29] Y. Andreopoulos, M. Gong, Z. Wang, S. Xanthos, A probe to measure direction and strength of moving shocks or blast waves, American Institute of Aeronautics and Astronautics Journal 41 (2003) 476–484.
[30] Z. Han, X. Yin, Shock Dynamics, Springer, 1993.
[31] B. Van Leer, Towards the ultimate conservative difference scheme. V. A second-order sequel to Godunov's method, Journal of Computational Physics 32 (1) (1979) 101.
[32] A. Harten, High resolution schemes for hyperbolic conservation laws, Journal of Computational Physics 49 (3) (1983) 357.
[33] A. Harten, B. Engquist, S. Osher, S.R. Chakravarthy, Uniformly high order accurate essentially non-oscillatory schemes, iii, Journal of Computational Physics 131 (1) (1997) 3.
[34] G.-S. Jiang, C.-W. Shu, Efficient implementation of weighted ENO schemes, Journal of Computational Physics 126 (1) (1996) 202.
[35] M.S. Darwish, F. Moukalled, Tvd schemes for unstructured grids, International Journal of Heat and Mass Transfer 46 (4) (2003) 599.
[36] M.E. Hubbard, Multidimensional slope limiters for MUSCL-type finite volume schemes on unstructured grids, Journal of Computational Physics 155 (1) (1999) 54.
[37] T.J. Barth, Higher order solution of the Euler equations on unstructured grids using quadratic reconstruction, in: 28th Aerospace Sciences Meeting, vol. 90-0013, Reno Nevada, 1990, AIAA paper.
[38] T.J. Barth, D.C. Jespersen, The design and application of upwind schemes on unstructured meshes, in: 27th Aerospace Sciences Meeting, vol. 89-0366, Reno, Nevada, 1989, AIAA Paper.
[39] N. Frink, Recent progress toward a three dimensional unstructured Navier–Stokes flow solver, 94-0061, 1994, AIAA Paper.
[40] D.J. Mavriplis, Unstructured mesh generation and adaptivity, in: VKI Lect. Ser. Comput. Fluid Dyn., vol. 26th, 1995.
[41] M. Sun, Numerical and Experimental Studies of Shock Wave Interaction with Bodies. Ph.D. Thesis, Tohoku University, 1998.
[42] D.J. Mavriplis, Unstructured grid techniques, Annual Review of Fluid Mechanics 29 (1) (1997) 473–514.
[43] B.G. Baumgart, Geometric Modelling for Computer Vision. Ph.D. Thesis, 1974.
[44] C.M. Eastman, Introduction to computer aided design, course notes, 1982.
[45] J.M. Legakis, K. Raj, Data structures for unstructured meshes, course notes, 2000.
[46] G. Berti. Generic Software Components for Scientific Computing. Ph.D. Thesis, Faculty of Mathematics, Computer Science and Natural Science, BTU Cottbus, Germany, 2000.
[47] P. Heckbert, Quad edge data structure and library, 2001.
[48] R. Lohner, Mesh adaptation in fluid mechanics, Engineering Fracture Mechanics 50 (5–6) (1995) 819.
[49] R. Lohner, An adaptive finite element scheme for transient problems in cfd, Computer Methods in Applied Mechanics and Engineering 61 (3) (1987) 323.